JOURNAL OF PETROLOGY | VOLUME 46 | NUMBER 10 | PAGES 2023–2058 | 2005 | doi:10.1093/petrology/egi046

Experimental Constraints on the Role of Garnet Pyroxenite in the Genesis of High-Fe Mantle Plume Derived Melts

J. TUFF[1]*, E. TAKAHASHI[2,3] AND S. A. GIBSON[1]

[1]DEPARTMENT OF EARTH SCIENCES, UNIVERSITY OF CAMBRIDGE, DOWNING STREET, CAMBRIDGE CB2 3EQ, UK

[2]DEPARTMENT OF EARTH AND PLANETARY SCIENCES, TOKYO INSTITUTE OF TECHNOLOGY, MEGURO, TOKYO 152-8551, JAPAN

[3]INSTITUTE FOR RESEARCH ON EARTH EVOLUTION, JAMSTEC, YOKOSUKA, JAPAN

RECEIVED SEPTEMBER 30, 2004; ACCEPTED APRIL 1, 2005
ADVANCE ACCESS PUBLICATION MAY 6, 2005

The anhydrous phase relations of an uncontaminated (primitive), ferropicrite lava from the base of the Early Cretaceous Paraná–Etendeka continental flood basalt province have been determined between 1 atm and 7 GPa. The sample has high contents of MgO (~14·9 wt %), FeO (14·9 wt %) and Ni (660 ppm). Olivine phenocrysts have maximum Fo contents of 85 and are in equilibrium with the bulk rock, assuming a* $K_{DFe-Mg}^{Ol-liquid}$ *of 0·32. A comparison of our results with previous experimental studies of high-Mg rocks shows that the high FeO content of the ferropicrite causes an expansion of the liquidus crystallization field of garnet and clinopyroxene relative to olivine; orthopyroxene was not observed in any of our experiments. The high FeO content also decreases solidus temperatures. Phase relations indicate that the ferropicrite melt last equilibrated either at ~2·2 GPa with an olivine–clinopyroxene residue, or at ≥5 GPa with a garnet–clinopyroxene residue. The low bulk-rock* Al_2O_3 *content (9 wt %) and high* $[Gd/Yb]_n$ *ratio (3·1) are consistent with the presence of residual garnet in the ferropicrite melt source and favour high-pressure melting of a garnet pyroxenite source. The garnet pyroxenite may represent subducted oceanic lithosphere entrained by the upwelling Tristan starting mantle plume head. During adiabatic decompression, intersection of the garnet pyroxenite solidus at ~5 GPa would occur at a mantle potential temperature of ~1550°C and yield a ferropicrite primary magma. Subsequent melting of the surrounding peridotite at ~4·5 GPa may be restricted by the thickness of the overlying sub-continental lithosphere, such that dilution of the garnet pyroxenite melt component would be significantly less than in intra-oceanic plate settings (where the lithosphere is thinner). This model may explain the limited occurrence of ferropicrites at the base of continental flood basalt sequences and their apparent absence in ocean-island basalt successions.*

KEY WORDS: *continental flood basalt; ferropicrite; mantle heterogeneity; mantle melting; phase relations; pyroxenite*

INTRODUCTION

Partial melts derived from the high-temperature axes of Phanerozoic mantle plumes are considered to be high-Mg picritic basalts (>12 wt % MgO), whereas melts from the cooler entrained (upper?) mantle in the peripheral regions of the plume head are lower temperature basaltic magmas (e.g. Campbell & Griffiths, 1990, 1993; Herzberg, 1995). Samples of the former should retain the most information about the intrinsic composition of the mantle plume source, if they escape subsequent contamination by lithospheric (crust or mantle) melts en route to the surface. Picritic magmas from both oceanic and continental intra-plate settings are characterized by FeO* (where FeO* indicates total Fe) contents ranging from 9 to 13 wt % at ~15 wt % MgO. These melts are in equilibrium with olivine varying in composition from Fo_{88} to Fo_{90}, consistent with partial melting of a dominantly peridotitic source, similar in composition to experimental melts of fertile peridotite, such as KLB-1 (Fig. 1; e.g. Takahashi, 1986; Takahashi *et al.*, 1993). Nevertheless, it has been suggested that mantle plume starting heads composed only of peridotite could not generate the significant volumes of melts seen in large igneous provinces and that an eclogite or pyroxenite component is needed (Cordery *et al.*, 1997; Campbell, 1998; Takahashi *et al.*, 1998; Yaxley, 2000; Leitch & Davies, 2001).

*Corresponding author. Telephone: +44-1223-333400. Fax: +44-1223-333450. E-mail: jtuf02@esc.cam.ac.uk

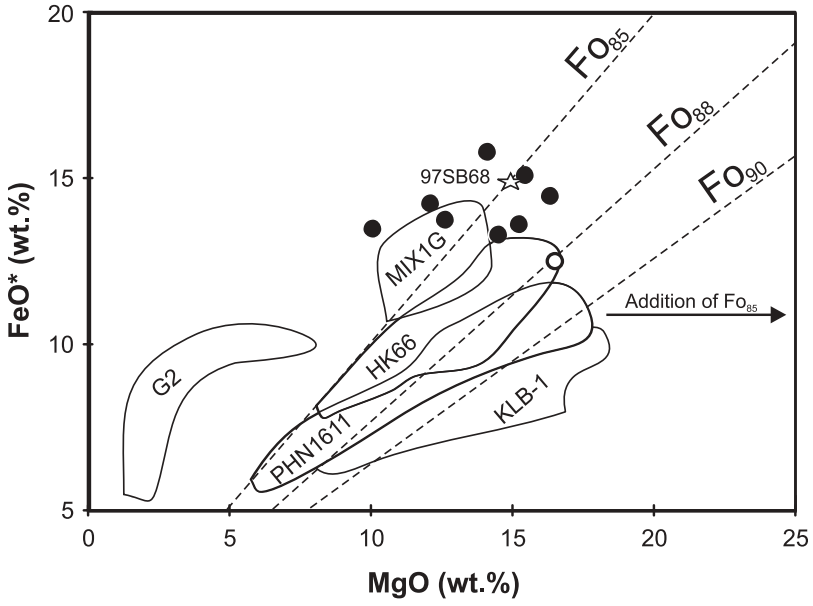

Fig. 1. Comparison of MgO and FeO* contents of ferropicrite 97SB68 (open star) with melts of peridotites KLB-1 (Takahashi, 1986; Takahashi *et al.*, 1993) and PHN-1611 (Kushiro, 1996), olivine websterite HK66 (Takahashi & Kushiro, 1983; Hirose & Kushiro, 1993), quartz eclogite G2 (Pertermann & Hirschmann, 2003*a*, 2003*b*) and silica-undersaturated garnet pyroxenite MIX1G (Kogiso *et al.*, 2003). Also shown (○) is the melt composition of a mixture of a 50:50 basalt–peridotite starting material ($GA1_{50}MPY90_{50}$; Yaxley & Green, 1998; Yaxley, 2000). •, Compositions of other ferropicrites from the Paraná–Etendeka CFB province (Gibson *et al.*, 2000).

There is convincing evidence that the Earth's mantle is not simply composed of peridotite. Some of the compositional variation in the mantle is believed to result from subduction of oceanic lithosphere (Allègre & Turcotte, 1986); however, the origins and extent of the heterogeneities, and their effects on deep-seated Earth processes, are poorly understood. Seismic data reveal variations in mantle velocity structure down to the core–mantle boundary (e.g. Silver *et al.*, 1988; Kaneshima & Helffrich, 1998, 1999; Kellogg *et al.*, 1999; Helffrich & Wood, 2001) and seismic tomographic images provide insight into the nature of mantle plumes (e.g. Zhao, 2001). Evidence for the existence of heterogeneous or 'marble cake' convecting mantle (Allègre *et al.*, 1980) may be also provided by rare, high-MgO (∼15 wt %) primitive magmas with anomalously high abundances of FeO* (∼13·5 to 16 wt %; Gibson *et al.*, 2000; Gibson, 2002). These high-Fe mantle melts (ferropicrites) occur infrequently in large igneous provinces (LIPs; e.g. Deccan, Ethiopia and Paraná–Etendeka), and some have incompatible trace-element and Sr–Nd–Pb isotope ratios that resemble those of ocean-island basalts (OIB). This suggests that they are predominantly derived from the convecting mantle (Gibson *et al.*, 2000). The ferropicrites are mildly alkaline to sub-alkaline (compare basanites and nephelinites, which also sometimes have high FeO, but have higher K_2O and Na_2O contents) and have low contents of Al_2O_3 (<10 wt %) and heavy rare earth elements (HREE; e.g. Lu <0·18 ppm); this is consistent with the derivation from a mantle source in which garnet is a residual phase. It has been proposed that the source of the high FeO* may be partial melting of garnet pyroxenite 'streaks' in the mantle derived from subducted mafic oceanic crust (Gibson *et al.*, 2000).

In this study we have undertaken a series of high-pressure melting experiments on a ferropicrite from the Paraná–Etendeka continental flood basalt (CFB) province in NW Namibia [sample 97SB68 from Gibson *et al.* (2000)]. Seventy-five experiments were performed over a wide range of temperatures (1000–1750°C) and pressures (1 atm–7 GPa) to constrain the phase relations at conditions appropriate to those in upwelling mantle plumes. The main aim of the experiments was to establish the conditions under which the Paraná–Etendeka ferropicrites were generated and to gain further insight into the composition of the ferropicrite source.

EXPERIMENTS

Starting material

Sample 97SB68 was collected from a ferropicrite lava flow at the base of the Paraná–Etendeka CFB succession in NW Namibia (Gibson *et al.*, 2000). An $^{40}Ar/^{39}Ar$ age of 132 ± 0·7 Ma has been determined for the flow (Renne *et al.*, 1997) and it has been associated with the Early Cretaceous impact of the Tristan da Cunha mantle plume on the base of the lithosphere (Gibson *et al*, 2000;

Table 1: Compositions (in wt %) of basalts, picrites and komatiites used in high-pressure melting experiments

	97SB68	N5	GR67	183-15	C520	CRB72-31	59-P-13	NG 7621	M620	HSS-15
SiO_2	46·91	48·20	45·51	48·43	45·90	49·17	47·76	48·7	45·60	46·77
TiO_2	1·75	3·04	1·93	1·60	1·80	3·15	3·03	0·42	0·40	0·33
Al_2O_3	9·09	10·10	12·44	9·96	11·7	14·45	14·93	8·44	7·95	3·42
FeO*	14·90	9·18	9·54	10·84	12·5	13·91	13·74	12·0	12·66	11·26
MnO	0·17	0·15	0·15	0·17	0·20	0·19	0·20	0·19	0·20	0·19
MgO	14·94	12·50	18·79	18·24	16·5	5·70	6·70	20·4	25·00	31·51
CaO	8·08	8·54	9·67	8·00	8·40	8·94	9·41	8·58	7·60	5·67
Na_2O	1·94	1·97	1·64	1·93	2·10	2·54	2·62	0·39	0·01	0·08
K_2O	0·68	1·87	0·08	0·25	0·50	1·01	0·75	–	0·02	0·08
P_2O_5	0·19	0·44	0·20	0·16	0·20	0·65	0·53	0·04	–	–
NiO	0·08	–	–	–	–	–	–	0·13	–	–
Cr_2O_3	–	–	–	–	0·20	–	–	0·43	–	–
Total	100·31	99·70	100·00	99·58	100·00	99·71	99·70	98·89	100·00	100·00
Mg-no.	64	71	78	75	70	42	46	75	78	83

Mg-no. = 100[Mg/(Mg + Fe^{2+})]. 97SB68, ferropicrite, Paraná–Etendeka CFB province (Gibson *et al.*, 2000); N5, picrite, Karoo CFB province (Cox & Jamieson, 1974); GR67, synthetic picrite (Green & Ringwood, 1967); 183-15, picrite with 2 wt % $Fo_{91·22}$ added, Hawaii (Maaløe, 2004); C520, picritic melt from $GA1_{50}MPY90_{50}$ (Yaxley & Green, 1998); CRB72-31, basalt, Columbia River CFB province (Takahashi *et al.*, 1998); 59-P-13, basalt, Snake River Plain, Idaho (Thompson, 1975); NG 7621, aluminium-undepleted komatiite, Belingwe (Bickle *et al.*, 1977); M620, aluminium-undepleted komatiite, Munro Township (Wei *et al.*, 1990); HSS-15, aluminium-depleted komatiite, Barberton (Wei *et al.*, 1990).
*Total Fe expressed as FeO.

Thompson *et al.*, 2001). Sample 97SB68 was chosen as the starting material in our experiments because it is petrographically fresh, has a low loss-on-ignition value (0·43 wt %), and has high contents of MgO (14·94 wt %), FeO* (14·90 wt %) and NiO (0·08 wt %; Table 1). It is among the most magnesian of the Paraná–Etendeka ferropicrites (Fig. 2). It has significantly higher FeO than other high-MgO rocks from the CFB province. Of the samples that have higher MgO contents than 97SB68, the Horingbaai types were considered by Thompson *et al.* (2001) to have accumulated olivine, whereas those from Gibson *et al.* (1995, 1996) were considered to have been derived from veined lithospheric mantle, rather than the convecting mantle. The ferropicrite contains olivine phenocrysts that are more Fe-rich (Fo_{85}) than those from picrites worldwide (Fig. 1; Gibson *et al.*, 2000). Using a $K_{DFe-Mg}^{Ol-liquid}$ of 0·32 (Ulmer, 1989), the olivine is in equilibrium with the bulk-rock Mg-number of 65 [where Mg-number = Mg/(Mg + Fe^{2+})]; this suggests that the bulk-rock composition of the ferropicrite has not undergone significant modification by olivine fractionation or accumulation since melt generation (Fig. 1). Addition or removal of equilibrium olivine (Fo_{85}) from the melt would produce minor variations in FeO*, relative to MgO, but cannot explain the high FeO* contents of the Paraná–Etendeka ferropicrites. Furthermore, the olivine phenocrysts from the Paraná–Etendeka ferropicrites have relatively high Ni contents and low Fo contents (Fo_{85}; see Gibson, 2002, fig. 6). The Ni contents of olivines may also be controlled by fractionation, but Fig. 3 shows that the ferropicrite olivines do not plot on fractionation trends defined by other Paraná–Etendeka samples (Horingbaai and Brandberg), or OIB and mid-ocean ridge basalt (MORB) picrites. Plagioclase crystallization could also cause an increase in melt FeO* content but this phase is present only in the groundmass. We conclude that 97SB68 is among the most primitive of the Paraná–Etendeka lavas, has not undergone modification by olivine accumulation or fractionation and is therefore an appropriate starting material for our study.

Experimental and analytical procedures

All experiments were performed in the Experimental Petrology Laboratory (Magma Factory), at Tokyo Institute of Technology (Takahashi *et al.*, 1993). Melting phase relations as well as the compositions and modal proportions of all coexisting phases were successfully determined in 60 of the run products. Prior to undertaking the experiments, a small amount of the 97SB68 starting material (~1 g) was fired at 1000°C in a CO_2–H_2 gas mixture at $\log fO_2$ = QFM (where QFM is the quartz–fayalite–magnetite buffer) for 2 h to ensure

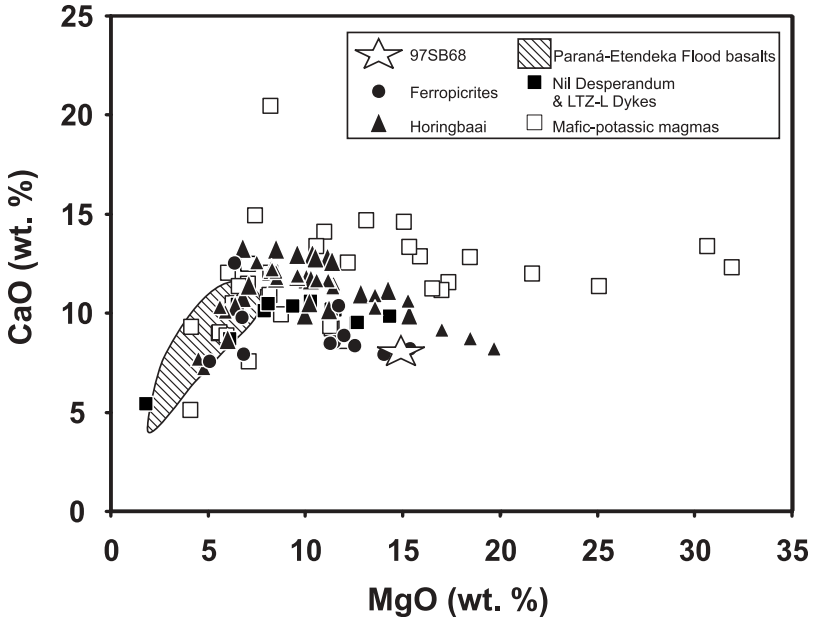

Fig. 2. Comparison of bulk-rock MgO and CaO contents of ferropicrite 97SB68 with other magma compositions from the Paraná–Etendeka CFB province: ferropicrites (Gibson *et al.*, 2000); Horingbaai lavas (Thompson & Gibson, 2000; Thompson *et al.*, 2001); Nil Desperandum and LTZ-L dykes (Thompson *et al.*, 2001); mafic–potassic magmas (Gibson *et al.*, 1995, 1996); Paraná–Etendeka continental flood basalts (hatched field; Peate, 1990).

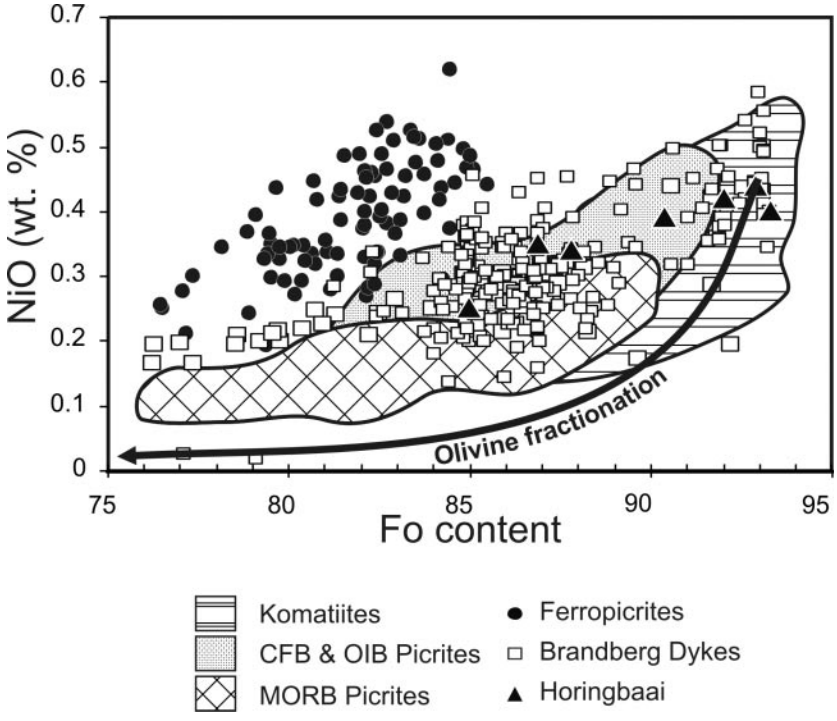

Fig. 3. Fo content vs NiO (wt %) for olivines in high-Mg magma compositions from the Paraná–Etendeka CFB province, worldwide komatiites, OIB picrites and MORB picrites. The olivine fractionation trend was calculated using the bulk-rock and olivine compositions of a Barberton komatiite. Data sources: Van Heerden & Le Roex (1988); Renner (1989); Kamenetsky *et al.* (1995); Baker *et al.* (1996); Garcia (1996); Parman *et al.* (1997); Gibson *et al.* (2000); Thompson *et al.* (2001); S. A. Gibson & R. N. Thompson (unpublished data, 2000).

complete dehydration. The powder was then ground in ethanol for several hours to produce uniformly fine grains, before drying for several days at 110°C. Experiments at 1 atm used a quenching furnace, with oxygen fugacity controlled at QFM using a CO_2–H_2 gas mixture. The starting material was suspended in the furnace on thin Pt wire (preformed by making a glass bead of the starting material fused on the wire at 1300°C) and quenched after the desired run duration by electrically cutting the wire and allowing the sample to drop through the furnace. Oxygen fugacity was controlled at QFM to create a balance between excessive Fe loss by alloying with the Pt wire [observed if the fO_2 was more reducing, i.e. MW (magnetite–wüstite)] and excessive formation of Fe_2O_3 (observed if the fO_2 was more oxidizing, i.e. normal atmospheric fO_2).

Experiments at pressures between 1·1 and 3 GPa were conducted using (1) a non-end-loaded ET-type (Matsukage & Kubo, 2003) and (2) an end-loaded Boyd–England-type piston-cylinder apparatus (e.g. Takahashi, 1986). All experiments used the 1/2-inch, talc Pyrex assembly of Takahashi & Kushiro (1983), consisting of a straight graphite heater and internal spacers of crushable MgO. All parts were fired at 1000°C in a 1 atm furnace, for 1 h prior to assembly, to ensure the removal of volatiles. The finely powdered sample was contained in a 4 mm length × 1·8 mm O.D. graphite capsule that was sealed within a Pt container. All temperatures were measured using $W_{95}Re_5$–$W_{74}Re_{26}$ thermocouples. The hot piston-in technique was employed for all experiments. Pressures were calibrated using the 1·6 GPa reaction Ab = Jd + Qz at 600°C (Holland, 1980) and the 2·97 GPa quartz–coesite transition at 1000°C (Bohlen & Boettcher, 1982). A pressure correction of −16% was thus applied (Takahashi, 1986).

Experiments between 5 and 7 GPa were undertaken using an SPI 1000 multi-anvil apparatus (e.g. Takahashi *et al.*, 1993). A MgO–Al_2O_3 (99:1 wt %) octahedron with 18 mm edge length was used as the pressure medium, with tungsten carbide anvils of 11 mm truncation edge length separated by pyrophyllite gaskets. The furnace assembly was similar to that used by Takahashi *et al.* (1993), and consisted of a straight $LaCrO_3$ heater, a ZrO_2 outer sleeve and MgO inner spacers. The sample powder was contained in a graphite capsule of 2·5 mm length × 1·8 mm O.D., sealed in a Pt container. All furnace parts and pressure media were fired in a furnace at 1000°C for 1 h prior to assembly and then stored in a vacuum oven at 220°C overnight. $W_{95}Re_5$–$W_{74}Re_{26}$ thermocouples were used throughout. Pressure was calibrated at room temperature using transformations of Bi (I–II and II–V) and at 1200°C using the transition of Fe_2SiO_4 in olivine to spinel. All piston cylinder and multi-anvil experimental runs were quenched after the desired duration by turning off the power to the graphite or $LaCrO_3$ heaters while maintaining run pressure, which was subsequently slowly released.

The run products were sectioned longitudinally and mounted in epoxy before polishing and examination with an optical microscope. An assessment of the position of the run capsule with respect to the thermocouple and the hottest part of the heater was then made (see below). The run products were analysed with a JEOL JXA8800 electron microprobe at Tokyo Institute of Technology. Wavelength-dispersive spectrometry (WDS) analyses were conducted using a 15 kV accelerating voltage and $1{\cdot}20 \times 10^{-8}$ A beam current. Peak acquisition times of 10 s were employed for Na, 20 s for Al, Ca, Cr, Fe, K, Mg, Si and Ti, and 30 s for Mn, Ni and P. On-line corrections were performed using LINK Analytical ZAF software.

Estimation of errors in temperature and pressure

For the 1 atm experiments the temperature distribution throughout the furnace was calibrated prior to the experimental runs. The hottest part of the furnace extended over 20 mm in the centre and this position was achieved for each 1 atm run. Because the run charges were ≤3 mm in diameter, temperature gradients were negligible and errors ∼ ±2°C.

The pressure uncertainty in the multi-anvil experiments was estimated to be <0·5 GPa and <0·1 GPa for piston-cylinder experiments (Takahashi & Kushiro, 1983; Takahashi, 1986; Takahashi *et al.*, 1993). No pressure correction was made on the e.m.f. of the thermocouple (Takahashi *et al.*, 1993). Temperatures were controlled to within ±2°C for both piston-cylinder and multi-anvil experiments. Thermal gradients are known to be high for graphite and higher still for $LaCrO_3$ heaters (Takahashi *et al.*, 1982), and cause the largest sources of error. They were calculated using pyroxene geothermometer mapping in a similar way to that proposed by Takahashi *et al.* (1982). Temperature gradients are estimated to be ≤15°C/mm in both ET-type and Boyd–England-type experiments. Multi-anvil experiments had thermal gradients of ≤40°C/mm, which equates to an uncertainty of <40°C as all charges examined were located within 1 mm (usually <0·5 mm) of the thermocouple junctions.

EXPERIMENTAL RESULTS

Phase assemblages

Details of the experimental run conditions and phase assemblages are summarized in Table 2. The liquidus phase relations and location of the nominally anhydrous solidus of ferropicrite 97SB68 are shown in Fig. 4a. The liquidus phase was found to be olivine up to ∼2·2 GPa, then clinopyroxene, which was replaced by garnet at

Table 2: Experimental run conditions

Run no.	Apparatus	Pressure (GPa)	Temperature (°C)	Duration (h)	Run products
J 12	1 atm furnace	0·0001	1100	24	ol, plag, cpx, melt
J 9	1 atm furnace	0·0001	1125	24	ol, plag, cpx, melt
J 8	1 atm furnace	0·0001	1150	24	ol, plag, melt
J 7	1 atm furnace	0·0001	1175	24	ol, melt
J 6	1 atm furnace	0·0001	1200	24	ol, melt
J 5	1 atm furnace	0·0001	1225	24	ol, melt
J 4	1 atm furnace	0·0001	1250	24	ol, melt
J 1	1 atm furnace	0·0001	1275	24	ol, melt
J 2	1 atm furnace	0·0001	1300	24	ol, melt
J 3	1 atm furnace	0·0001	1325	24	ol, melt
J 10	1 atm furnace	0·0001	1350	24	ol, melt
J 11	1 atm furnace	0·0001	1375	24	melt
P 520	BE piston	1·1	1200	24	ol, plag, cpx, melt
P 517	BE piston	1·1	1225	24	ol, cpx, melt
AK 96	K2 piston	1·1	1250	4	ol, cpx, melt
AK 94	K2 piston	1·1	1275	4	ol, cpx, melt
AK 92	K2 piston	1·1	1300	4	ol, cpx, melt
AK 90	K2 piston	1·1	1350	2	ol, melt
AK 88	K2 piston	1·1	1400	2	ol, melt
P 521	BE piston	1·1	1425	24	melt
P 527	BE piston	1·1	1425 (1 h)–1325 (12 h)*	25	ol, melt
P 519	BE piston	1·5	1250	24	ol, cpx, melt
P 518	BE piston	1·5	1275	24	ol, cpx, melt
AK 101	K2 piston	1·5	1300	4	ol, cpx, melt
AK 100	K2 piston	1·5	1350	4	ol, cpx, melt
AK 99	K2 piston	1·5	1400	4	ol, melt
AK 98	K2 piston	1·5	1425	4	ol, melt
AK 97	K2 piston	1·5	1450	4	ol, melt
AK 102	K2 piston	2	1300	4	ol, cpx, melt
AK 103	K2 piston	2	1350	4	ol, cpx, melt
P 513	BE piston	2	1400	24	ol, cpx, melt, (qc)
P 514	BE piston	2	1450	24	melt, (qc)
P 515	BE piston	2	1475	24	melt
P 516	BE piston	2	1500	24	melt
P 530	BE piston	2·5	1450	12	cpx, ol, melt, (qc)
P 531	BE piston	2·5	1475	12	cpx, melt, (qc)
P 508	BE piston	3	1400	24	cpx, grt, ol
P 512	BE piston	3	1450	24	cpx, grt, ol, (qc)
P 511	BE piston	3	1475	24	cpx, grt, (qc)
P 507	BE piston	3	1500	24	cpx, (qc)
P 510	BE piston	3	1525	24	cpx, (qc)
P 509	BE piston	3	1550	24	(qc)
P 529	BE piston	3	1525 (1 h)–1425 (12 h)*	25	cpx, grt, ol, melt
S 1291	SPI 1000	5	1400	4	cpx, grt, ol
S 1318	SPI 1000	5	1450	4	cpx, grt, ol, melt
S 1295	SPI 1000	5	1500	4	cpx, grt, melt, (qc)
S 1315	SPI 1000	5	1500	4	cpx, grt, melt, (qc)
S 1308	SPI 1000	5	1550	4	cpx, grt, melt, (qc)

Run no.	Apparatus	Pressure (GPa)	Temperature (°C)	Duration (h)	Run products
S 1300	SPI 1000	5	1600	4	cpx, grt, (qc)
S 1314	SPI 1000	5	1600	4	cpx, grt, (qc)
S 1317	SPI 1000	5	1650	4	melt, (qc)
S 1333	SPI 1000	6	1625	4	grt, cpx, melt
S 1328	SPI 1000	7	1450	4	grt, cpx, ol
S 1327	SPI 1000	7	1500	4	grt, cpx, ol, (qc)
S 1324	SPI 1000	7	1550	4	grt, cpx, ol, (qc)
S 1323	SPI 1000	7	1600	4	grt, cpx, (qc)
S 1320	SPI 1000	7	1650	4	grt, cpx, (qc)
S 1319	SPI 1000	7	1700	4	grt, cpx, melt, (qc)
S 1330	SPI 1000	7	1750	4	grt, cpx, melt

ol, olivine; plag, plagioclase; cpx, clinopyroxene; grt, garnet; (qc), quench crystals.
*Reverse runs starting from melt and cooling to desired temperature.

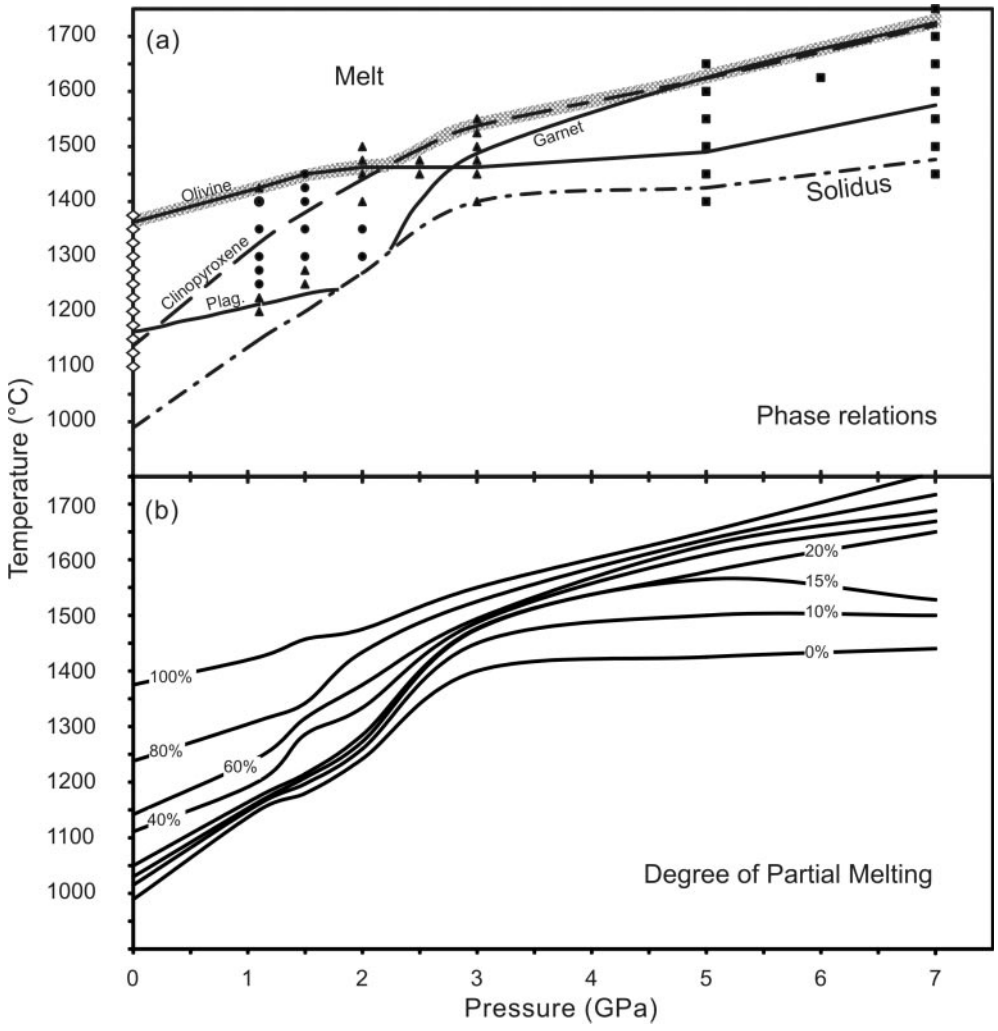

Fig. 4. (a) Phase relations of ferropicrite 97SB68. Data points are from experiments using: (1) 1 atm furnace (◇); (2) K2-type piston cylinder apparatus (●); (3) Boyd–England type piston cylinder apparatus (▲); (4) SPI-1000 multi-anvil apparatus (■). Thick shaded line indicates the ferropicrite liquidus. (b) Degree of partial melting of 97SB68 determined by X-ray mapping analysis and mass-balance calculations.

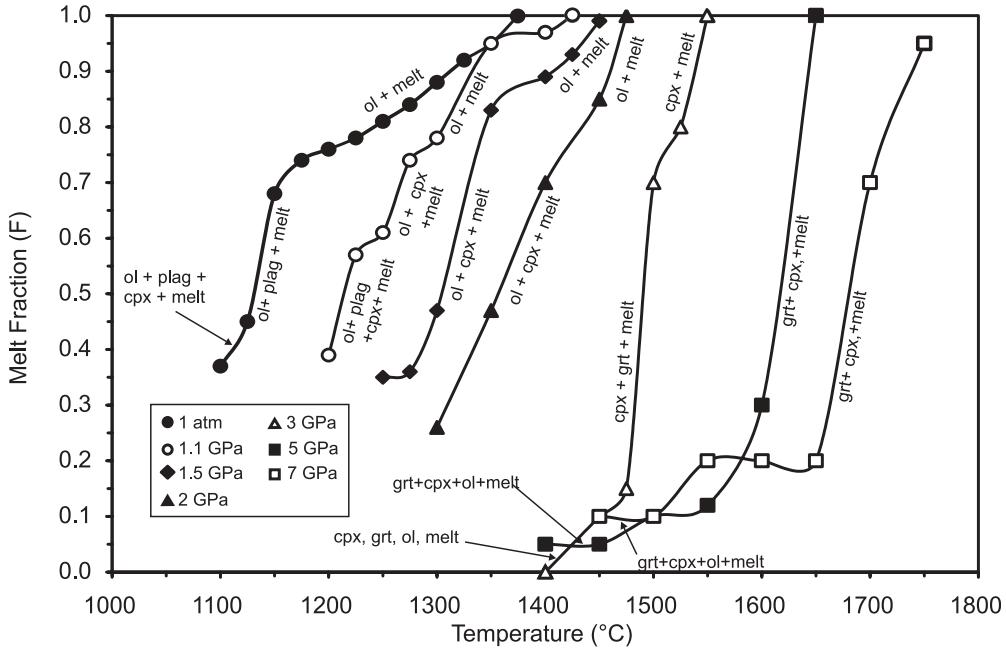

Fig. 5. Degree of partial melting expressed as melt fraction for 1 atm to 7 GPa runs. The degree of partial melting of 97SB68 was determined by X-ray mapping analysis and mass-balance calculations. Approximate appearances of phases are shown and are abbreviated as follows: ol, olivine; plag, plagioclase; cpx, clinopyroxene; grt, garnet.

5 GPa. Orthopyroxene and spinel were not observed in any of the experiments; the absence of the latter is possibly due to the low Cr content of the starting material compared with picrites worldwide (Gibson *et al.*, 2000). The liquidus at 2·2 and 5 GPa is at ~1450°C and ~1625°C, respectively. Clinopyroxene and olivine are observed as subsolidus phases over the entire range of the experiments. We observed plagioclase up to 1·1 GPa, but not in experimental runs at 1·5 GPa. However, 1·5 GPa experimental runs did not cover the ferropicrite solidus and it is inferred (by extrapolation) that plagioclase may be stable up to ~1·75 GPa, with garnet found from ~2·2 GPa. At 1 atm, olivine crystallized below 1375°C. A large crystallization interval exists between this and the appearance of plagioclase, which was observed at 1150°C, with clinopyroxene present below 1150°C (Fig. 4a).

At 3 GPa, the subsolidus assemblage is clinopyroxene, garnet and olivine. A marked inflection is seen in the solidus, just below 3 GPa (see below). Although clinopyroxene is replaced by garnet as the liquidus phase around 5 GPa, their relative order of crystallization is extremely close and garnet and cpx are effectively cotectic. Figures 4b and 5 show the relationship between the degree of partial melting, temperature and pressure for the experimental runs; back-scattered electron images of sections through the experimental charges at 1 atm, 3 GPa, 5 GPa and 7 GPa are shown in Figs 6 and 7. For experiments below 3 GPa, the increase in the degree of partial melting with increasing temperature is fairly gradual, with major inflections corresponding to the exhaustion of particular phases; for example, the inflections at around 1225°C and 1300°C for 1·1 GPa runs (Fig. 5) correspond to the disappearance of plagioclase and clinopyroxene, respectively. This behaviour can also be seen in the 1 atm runs (Fig. 6): the melt fraction gradually increases between 1100 and 1175°C, as clinopyroxene and plagioclase disappear and olivine remains as the liquidus phase. For experimental runs at 3 GPa and above, however, there is initially only a small increase in melt fraction above the solidus over a wide temperature range (≤200°C), followed by a large increase in degree of melting over the next 50–100°C (Figs 4b and 5). At 3 GPa, olivine and garnet disappear by 1475 and 1500°C, respectively, as the melt fraction rapidly increases and pyroxene becomes the liquidus phase (Fig. 6). In experiments at 5 GPa, the melt fraction stays below 0·1 until the charge has reached 1500°C and then the melt fraction rapidly increases to 1·0 at 1650°C. The inflection in the melt fraction curve that straddles 1450–1500°C at 5 GPa (Fig. 5) corresponds to the exhaustion of olivine. The melt fraction rapidly increases from 0·3 at 1600°C to 1 at 1650°C. Comparison with Fig. 4a shows that there is a large melting interval between the olivine-out line and the cotectic-like positions of pyroxene and garnet. Similar behaviour is seen at 7 GPa, where the melt fraction has increased from 0·2 to ~1 between 1650 and 1750°C and garnet is observed as the liquidus phase, but is closely associated with pyroxene (Fig. 7).

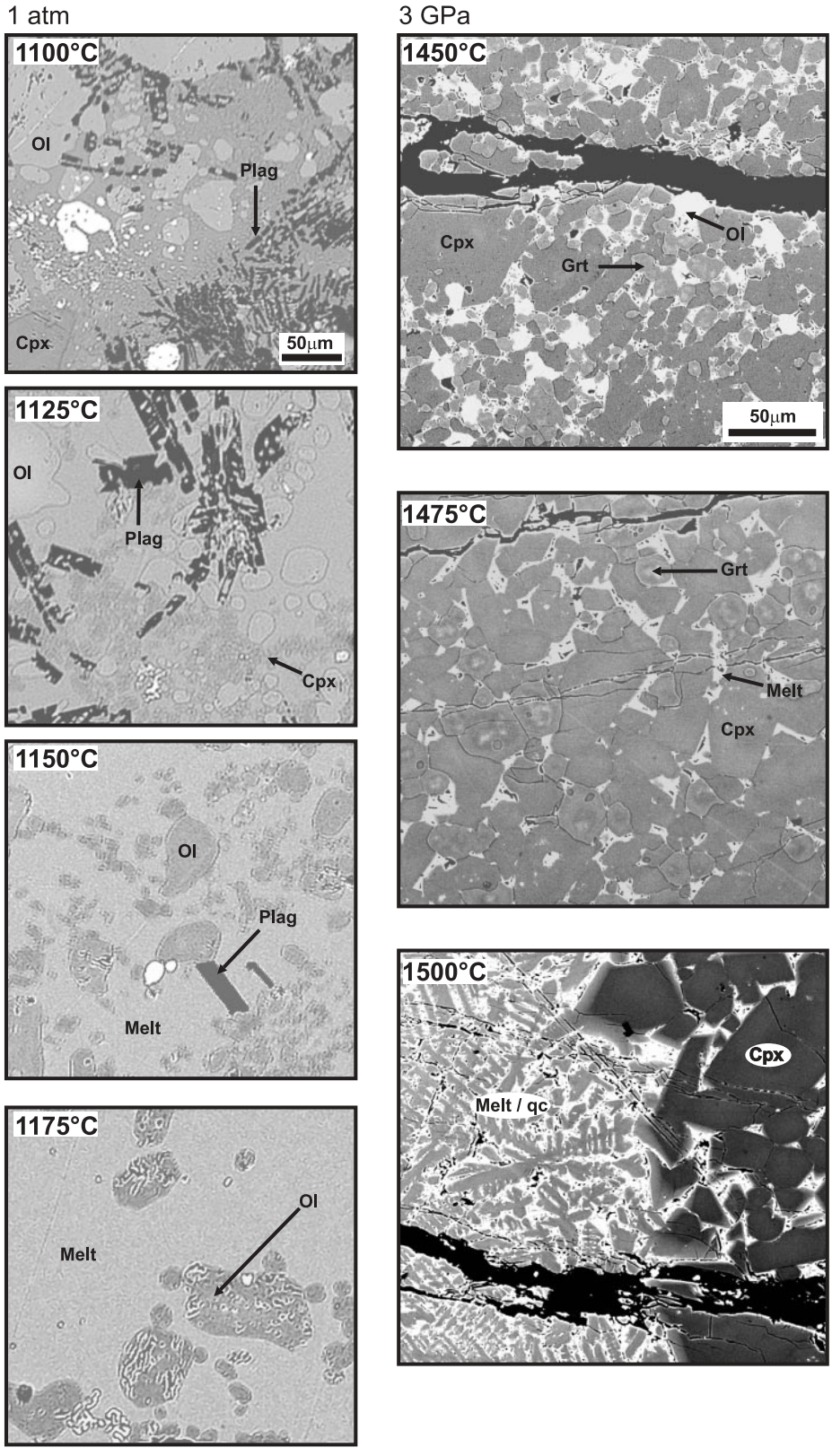

Fig. 6. Back-scattered electron images of sections through experimental charges at 1 atm and 3 GPa. Ol, olivine; Plag, plagioclase; Cpx, clinopyroxene; Grt, garnet; qc, quench crystals.

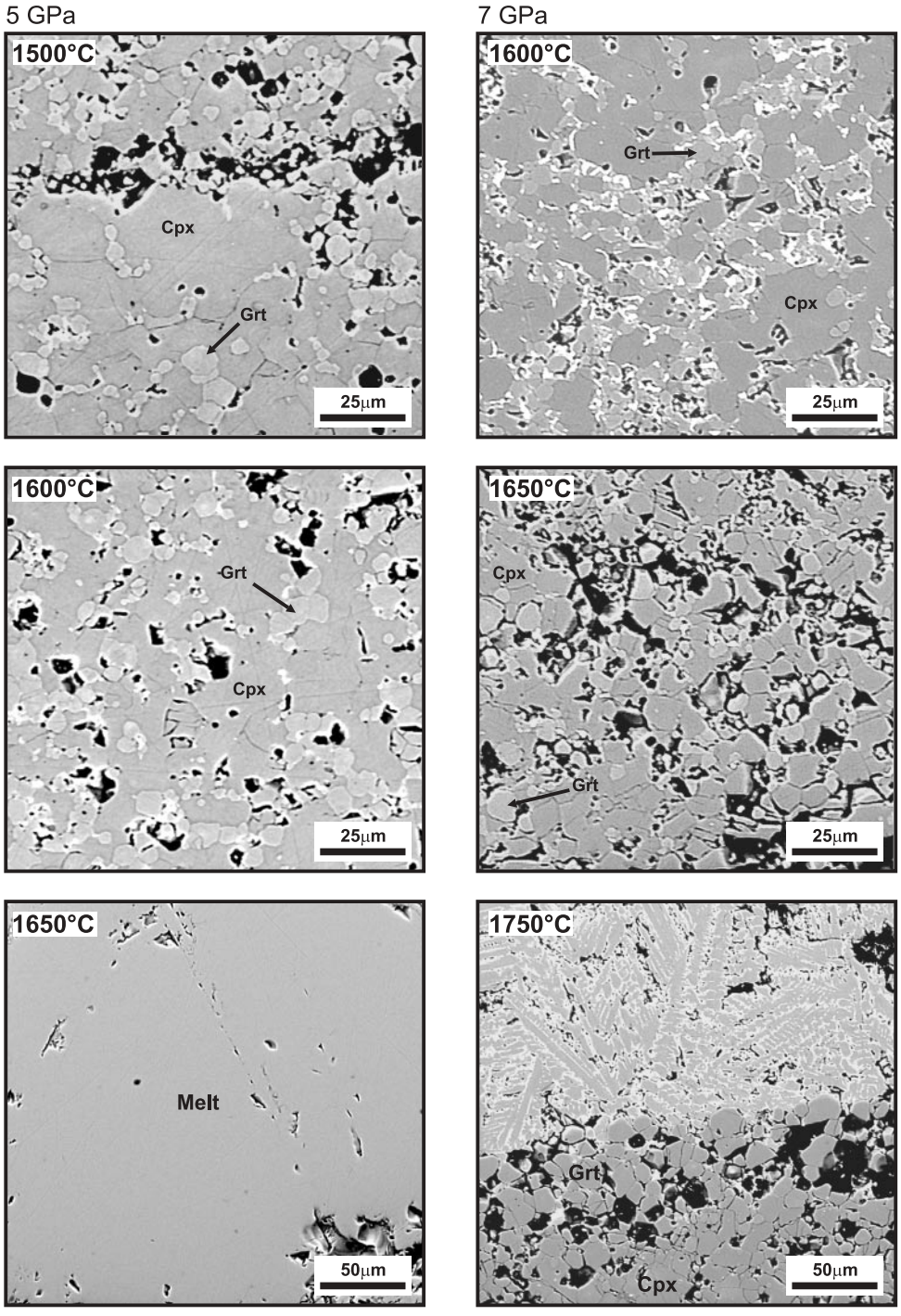

Fig. 7. Back-scattered electron images of sections through experimental charges at 5 GPa and 7 GPa. Abbreviations as for Fig. 6.

Quench crystals

At pressures above ~3 GPa, the observed partial melts are often present as acicular or dendritic quench crystals as well as quench glass. Melt compositions were analysed in a 20 μm^2 area using a beam scan technique. If the melt pockets were too small, for example in the interstitial regions between crystal phases, a ≤30 μm diameter defocused beam was used, which reduces the variability. Because of the heterogeneous quench crystal compositions, however, the high-pressure melt compositions have much larger uncertainty than the low-pressure ones (glasses).

Equilibrium

Run times for piston-cylinder and multi-anvil experiments (Table 2) are comparable with those of previous studies (e.g. Walter, 1998; Pertermann & Hirschmann, 2003*a*). Although 97SB68 is mafic, the bulk composition is high in alkalis (particularly K_2O, which is 0·68 wt % in 97SB68 and 0·09 wt % in KR4003) and we would expect 97SB68 melts to have relatively low viscosity and approach equilibrium relatively rapidly. Figures 6 and 7 show the textures of representative run products comprising equant euhedral crystal phases with homogeneous chemistry, indicating that equilibrium was achieved (Wang & Takahashi, 1999) over a wide range of pressures and temperatures. Relative standard deviations of Si, Fe and Mg in olivines are typically around 1–2 wt % (Table 3) and are comparable with microprobe uncertainty (e.g. Kogiso & Hirschmann, 2001). Fe–Mg partition coefficients (K_D) for olivine and melt are 0·28 ± 0·01 at 1 atm, 0·30 ± 0·03 at 1·1 GPa, 0·30 ± 0·04 at 1·5 GPa and 0·34 ± 0·02 at 2 GPa. $K_{DFe-Mg}^{Cpx-liquid}$ values for clinopyroxene and melt are 0·26 ± 0·02 at 1·1 GPa, 0·25 ± 0·04 at 1·5 GPa, 0·33 ± 0·02 at 2 GPa and 0·32 ± 0·03 at 2·5 GPa. For pressures ≥1·1 GPa, low K_D values are probably due to the presence of quench olivine and pyroxene crystals in the melt phase. The low $K_{DFe-Mg}^{Ol-liquid}$ value of the 1 atm run at 1125°C may be caused by Fe loss (see below). $K_{DFe-Mg}^{Gnt-liquid}$ values range from 0·42 to 0·48 (Table 3) and are comparable with those reported by Kogiso *et al.* (2003). The K_D values for all the phases in the 5 GPa runs are not within the accepted ranges (i.e. $K_{DFe-Mg}^{Ol-liquid} = \sim 0{\cdot}3$, $K_{DFe-Mg}^{Cpx-liquid} = \sim 0{\cdot}3$–$0{\cdot}4$ and $K_{DFe-Mg}^{Gnt-liquid} = \sim 0{\cdot}4$–$0{\cdot}5$; e.g. Takahashi & Kushiro, 1983; Walter, 1998). This may be due to errors in the determination of interstitial melt compositions (olivine is absent in near liquidus runs at this pressure) determined by averaging quench crystals (see above).

Although clinopyroxenes produced by melting natural starting materials are often reported to have un-reacted cores (relicts; e.g. Kogiso & Hirschmann, 2001), most of the clinopyroxenes analysed here, apart from those from the 1 atm runs, are homogeneous and show systematic compositional variations with temperature and pressure (see below). The experimental run at 1 atm and 1100°C is not thought to have reached equilibrium, despite a run duration of 24 h; olivine cores are more Fe-rich than rims, which may be due to Fe loss to the suspended Pt wire. Figure 6 shows that plagioclase and clinopyroxene are also poorly formed at this temperature, in contrast to the 1 atm run at 1125°C. Results from the 1 atm and 1100°C run have, therefore, been disregarded in subsequent analysis of the data.

Experimental runs were reversed for 1·1 and 3 GPa (P-527 and P-529, respectively; Table 2), to assess whether equilibrium had been achieved in the original experiments (i.e. comparing phases in experiments involving the progressive melting of the initial starting powder with the same phases crystallized in from the melt). At 3 GPa, the sample was heated above the liquidus at 1525°C for 1 h to ensure complete melting. The temperature was then lowered to 1425°C over 12 h and held at 1425°C for another 12 h before quenching. At 1·1 GPa, the same method was employed, with the sample initially held at 1425°C before cooling to 1325°C. Phases were found to be the same for both the progressive melting and crystallizing methods (e.g. the 1525 to 1425°C run at 3 GPa produced clinopyroxene, olivine, garnet and melt and is similar to the 1450°C experiment on the initial powdered starting material). Phase compositions were also similar for both the 1·1 and 3 GPa runs; run P-527, for example (1·1 GPa, 1425–1325°C), contained olivines that vary systematically with temperature in line with the general trend of 1·1 GPa olivines (Fig. 8; see below). It can be concluded that because the run products were the same whether the starting material was the initial powder or a melt, equilibrium had been closely approached for most experimental runs.

Compositions of crystalline phases

Electron microprobe analyses of the phases observed in each experimental run are reported in Table 3. At a given temperature, the olivines become less forsteritic with increasing pressure (Fig. 8). For all experimental pressures, the olivines show a general trend of increasing Fo with increasing temperature. NiO contents for olivines at pressure ≥1·1 GPa are unexpectedly low compared with those in olivines at 1 atm (Table 3). This is discussed below.

In all experiments, the garnet compositions are pyrope-rich (Fig. 9) and do not show major variations in CaO concentration (∼4·5 to ∼5·5 wt %; Fig. 8). The FeO* contents of the garnets increase with pressure (e.g. from ∼13·5 to 17 wt % at 1450°C and 3 and 7 GPa, respectively) and decreasing temperature and MgO content (Fig. 10). Na_2O and TiO_2 contents also increase with increasing pressure for a given temperature; for each pressure TiO_2 concentrations decrease with increasing temperature. A marked increase in TiO_2 concentration with falling temperature is observed for the lowest temperature experiments (≤1550°C) at 7 GPa. K_2O concentrations increase with pressure, for a given temperature and also increase with decreasing temperature, for a particular pressure. Conversely, the concentration of Al_2O_3 in the garnets decreases with increasing pressure (∼22 wt % at 3 GPa and 1450°C, compared with ∼20 wt % at 5 GPa and 1450°C and ∼19 wt % at 7 GPa and 1450°C) and increases with temperature for a given pressure. MgO contents also decrease with increasing pressure (∼17 wt % at 3 GPa and ∼14 wt %

Table 3: Phase compositions (in wt %) from all experimental runs

Run no.	T (°C)	n[1]	Phase[2]		SiO_2	TiO_2	Al_2O_3	FeO*	MnO	MgO	CaO	Na_2O	K_2O	NiO	P_2O_5	Cr_2O_3	Total	Mg-no.[3]	K_D[4]
1 atm																			
J-11	1375	3	melt	100	49·78	1·71	9·77	12·83	0·16	16·08	8·40	0·45	0·41	0·05	0·07	0·07	99·78	69	
					(0·28)	(0·05)	(0·18)	(0·20)	(0·01)	(0·20)	(0·09)	(0·01)	(0·02)	(0·03)	(0·01)	(0·01)			
J-10	1350	4	melt	99·5	49·77	1·84	9·74	12·56	0·16	15·69	8·61	0·70	0·44	0·01	0·11	0·15	99·79	69	
					(0·24)	(0·03)	(0·15)	(0·07)	(0·02)	(0·37)	(0·05)	(0·05)	(0·01)	(0·02)	(0·02)	(0·04)			
	1350	1	ol	0·5	41·55	0·06	0·07	11·23	0·07	48·48	0·27	0·01	0·00	0·11	0·00	0·07	101·91	88	0·29
J-3	1325	5	melt	95	49·15	1·90	10·02	13·66	0·20	13·87	8·87	1·39	0·58	0·05	0·15	0·11	99·95	64	
					(0·27)	(0·03)	(0·56)	(0·16)	(0·07)	(0·15)	(0·07)	(0·06)	(0·02)	(0·04)	(0·02)	(0·05)			
	1325	3	ol	5	40·90	0·02	0·08	12·94	0·09	46·78	0·28	0·01	0·00	0·27	0·00	0·10	101·47	87	0·28
					(0·35)	(0·03)	(0·01)	(0·11)	(0·08)	(0·19)	(0·04)	(0·01)	(0·00)	(0·04)	(0·00)	(0·03)			
J-2	1300	4	melt	90	49·03	2·00	10·52	13·79	0·16	12·23	9·30	1·62	0·65	0·06	0·18	0·14	99·68	61	
					(0·18)	(0·08)	(0·21)	(0·13)	(0·10)	(0·23)	(0·09)	(0·04)	(0·02)	(0·01)	(0·01)	(0·03)			
	1300	1	ol	10	41·06	0·03	0·06	14·16	0·18	45·71	0·28	0·01	0·01	0·28	0·00	0·10	101·87	85	0·27
J-1	1275	4	melt	84	49·11	2·08	11·01	13·55	0·13	10·90	9·53	2·15	0·78	0·04	0·21	0·10	99·58	59	
					(0·54)	(0·07)	(0·08)	(0·12)	(0·05)	(0·08)	(0·07)	(0·06)	(0·02)	(0·03)	(0·01)	(0·02)			
J-4	1250	4	melt	81	49·69	2·16	11·38	13·43	0·16	10·06	9·76	2·16	0·78	0·01	0·23	0·09	99·93	57	
					(0·25)	(0·05)	(0·04)	(0·07)	(0·07)	(0·18)	(0·08)	(0·05)	(0·04)	(0·01)	(0·02)	(0·02)			
	1250	2	ol	19	40·63	0·07	0·06	15·92	0·23	43·89	0·30	0·00	0·01	0·29	0·00	0·12	101·51	83	0·27
					(0·14)	(0·05)	(0·02)	(0·06)	(0·06)	(0·28)	(0·02)	(0·00)	(0·01)	(0·01)	(0·00)	(0·03)			
J-5	1225	4	melt	78	49·95	2·24	11·68	13·24	0·16	8·97	10·04	2·28	0·85	0·05	0·26	0·10	99·82	55	
					(0·27)	(0·09)	(0·28)	(0·28)	(0·01)	(0·24)	(0·06)	(0·06)	(0·04)	(0·04)	(0·02)	(0·02)			
J-6	1200	4	melt	76	50·49	2·31	12·38	11·84	0·15	7·02	10·68	2·41	0·90	0·03	0·27	0·06	98·54	51	
					(1·11)	(0·13)	(0·29)	(0·19)	(0·08)	(1·09)	(0·07)	(0·04)	(0·02)	(0·03)	(0·02)	(0·04)			
J-7	1175	5	melt	74	51·59	2·36	12·65	11·24	0·16	6·94	11·04	2·48	0·90	0·04	0·29	0·07	99·75	52	
					(0·28)	(0·05)	(0·15)	(0·19)	(0·04)	(0·06)	(0·23)	(0·07)	(0·03)	(0·05)	(0·01)	(0·02)			
J-8	1150	4	melt	66	51·79	2·59	13·81	11·11	0·13	5·69	10·27	2·85	1·07	0·01	0·32	0·03	99·65	48	
					(0·50)	(0·21)	(0·09)	(0·11)	(0·06)	(0·10)	(0·14)	(0·08)	(0·04)	(0·02)	(0·02)	(0·04)			
	1150	4	plag	n.d.	54·68	0·15	27·62	1·46	0·02	0·46	12·54	3·81	0·30	0·02	0·04	0·03	101·13	36	
					(1·22)	(0·11)	(0·88)	(0·52)	(0·01)	(0·28)	(0·75)	(0·40)	(0·06)	(0·02)	(0·03)	(0·03)			
J-9	1125	3	melt	47	51·34	4·03	13·25	11·93	0·13	4·68	9·12	3·23	1·42	0·05	0·44	0·04	99·67	41	
					(0·27)	(0·48)	(0·15)	(0·24)	(0·04)	(0·19)	(0·17)	(0·05)	(0·03)	(0·04)	(0·02)	(0·02)			
	1125	1	ol	32	39·06	0·03	0·02	24·72	0·29	36·94	0·30	0·01	0·00	0·32	0·00	0·05	101·74	73	0·26
	1125	3	plag	11	55·49	0·15	26·99	1·35	0·03	0·34	11·53	4·23	0·39	0·01	0·03	0·00	100·53	31	
					(0·71)	(0·08)	(0·46)	(0·10)	(0·02)	(0·09)	(0·49)	(0·28)	(0·03)	(0·01)	(0·01)	(0·00)			
	1125	4	cpx	9·9	50·76	1·63	4·32	8·88	0·14	14·82	19·59	0·39	0·05	0·04	0·11	0·34	101·06	75	0·23
					(1·11)	(0·61)	(0·16)	(0·49)	(0·05)	(0·25)	(0·23)	(0·09)	(0·07)	(0·04)	(0·02)	(0·09)			

Run no.	T (°C)	n[1]	Phase[2]		SiO_2	TiO_2	Al_2O_3	FeO*	MnO	MgO	CaO	Na_2O	K_2O	NiO	P_2O_5	Cr_2O_3	Total	Mg-no.[3]	K_D[4]
1·1 GPa																			
P-521	1425	15	melt	100	50·18	1·75	9·60	10·67	0·18	16·40	8·18	2·16	0·71	0·02	0·21	0·12	100·18	73	
					(0·26)	(0·07)	(0·10)	(0·19)	(0·06)	(0·23)	(0·10)	(0·07)	(0·02)	(0·02)	(0·02)	(0·03)			
AK-88	1400	5	melt	98	47·59	1·77	9·77	14·14	0·17	14·37	8·32	2·13	0·71	0·02	0·21	0·11	99·31	64	
					(0·30)	(0·07)	(0·15)	(0·17)	(0·02)	(0·16)	(0·08)	(0·09)	(0·03)	(0·03)	(0·01)	(0·04)			
	1400	1	ol	3	39·66	0·03	0·06	14·16	0·15	44·79	0·28	0·02	0·00	0·00	0·00	0·12	99·26	85	0·32
AK-90	1350	2	melt	95	48·30	1·98	10·64	13·90	0·20	11·55	9·30	2·21	0·70	0·01	0·24	0·15	99·18	60	
					(0·58)	(0·05)	(0·28)	(0·21)	(0·01)	(1·22)	(0·42)	(0·12)	(0·04)	(0·02)	(0·03)	(0·04)			
	1350	2	ol	5	39·48	0·01	0·05	16·48	0·21	43·52	0·33	0·03	0·00	0·07	0·00	0·07	100·25	82	0·31
					(0·54)	(0·01)	(0·00)	(0·39)	(0·01)	(0·15)	(0·01)	(0·00)	(0·00)	(0·05)	(0·00)	(0·03)			
AK-92	1300	1	cpx	n.d.	52·16	0·49	3·55	9·32	0·21	21·50	10·06	0·44	0·01	0·04	0·01	0·66	98·45	80	
AK-94	1275	1	melt	74	48·90	2·38	12·33	13·28	0·16	8·43	10·02	2·57	0·84	0·01	0·24	0·12	99·28	53	
	1275	1	ol	n.d.	38·91	0·07	0·05	19·56	0·19	40·78	0·34	0·02	0·00	0·10	0·00	0·00	100·02	79	0·30
AK-96	1250	2	cpx	n.d.	51·70	0·66	2·80	9·24	0·22	17·08	16·00	0·48	0·00	0·02	0·06	0·45	98·68	77	
					(0·94)	(0·14)	(0·72)	(1·29)	(0·02)	(2·95)	(5·39)	(0·06)	(0·00)	(0·02)	(0·04)	(0·18)			
P-517	1225	5	melt	57	49·19	2·61	14·22	13·71	0·18	6·87	8·54	3·25	1·16	0·00	0·36	0·06	100·14	47	
					(0·32)	(0·12)	(0·50)	(0·28)	(0·07)	(0·30)	(0·23)	(0·16)	(0·06)	(0·01)	(0·05)	(0·03)			
	1225	2	px	26	52·23	0·76	4·49	9·54	0·22	17·96	13·94	0·58	0·02	0·04	0·04	0·40	100·22	77	0·27
					(0·28)	(0·03)	(0·38)	(0·40)	(0·08)	(0·72)	(1·22)	(0·03)	(0·00)	(0·03)	(0·01)	(0·03)			
P-520	1200	3	melt	40	50·43	3·20	16·37	13·05	0·14	4·73	6·95	4·35	1·77	0·03	0·51	0·02	101·55	39	
					(0·76)	(0·14)	(0·22)	(0·47)	(0·01)	(0·48)	(0·13)	(0·11)	(0·07)	(0·05)	(0·01)	(0·02)			
	1200	2	ol	19	38·83	0·08	0·08	26·91	0·20	35·83	0·31	0·02	0·01	0·03	0·01	0·01	102·32	70	0·27
					(0·10)	(0·06)	(0·03)	(0·10)	(0·03)	(0·52)	(0·08)	(0·01)	(0·01)	(0·03)	(0·01)	(0·00)			
	1200	3	cpx	40	51·50	1·26	6·27	10·60	0·19	16·33	14·52	0·81	0·02	0·00	0·07	0·26	101·84	73	0·24
					(0·17)	(0·11)	(1·03)	(0·83)	(0·05)	(0·83)	(1·39)	(0·09)	(0·03)	(0·00)	(0·04)	(0·02)			
	1200	2	plag	1	56·71	0·14	27·62	0·71	0·03	0·14	10·26	5·16	0·60	0·03	0·03	0·00	101·43	25	
					(0·63)	(0·02)	(0·64)	(0·39)	(0·04)	(0·07)	(0·90)	(0·39)	(0·09)	(0·05)	(0·02)	(0·00)			
P-527	1425	10	melt	84	48·73	2·14	11·40	13·54	0·15	10·17	9·57	2·49	0·81	0·02	0·22	0·13	99·37	57	
					(0·33)	(0·05)	(0·22)	(0·14)	(0·05)	(0·27)	(0·10)	(0·05)	(0·03)	(0·02)	(0·02)	(0·03)			
	−1325	4	ol	16	39·44	0·05	0·08	17·92	0·17	42·56	0·31	0·02	0·01	0·01	0·00	0·10	100·66	81	0·32
					(0·32)	(0·03)	(0·01)	(0·38)	(0·06)	(0·86)	(0·02)	(0·02)	(0·01)	(0·02)	(0·00)	(0·03)			

Table 3: continued

Run no.	T (°C)	n[1]	Phase[2]		SiO_2	TiO_2	Al_2O_3	FeO*	MnO	MgO	CaO	Na_2O	K_2O	NiO	P_2O_5	Cr_2O_3	Total	Mg-no.[3]	K_D[4]
1·5 GPa																			
AK-97	1450	5	melt	97	48·01	1·77	9·66	14·20	0·15	14·30	8·36	2·07	0·70	0·01	0·20	0·12	99·56	64	
					(0·26)	(0·05)	(0·12)	(0·25)	(0·01)	(0·67)	(0·23)	(0·02)	(0·04)	(0·02)	(0·01)	(0·02)			
	1450	3	ol	3	40·18	0·06	0·10	14·37	0·10	44·59	0·31	0·04	0·03	0·01	0·00	0·10	99·90	85	0·32
					(0·38)	(0·02)	(0·02)	(0·05)	(0·06)	(0·60)	(0·03)	(0·02)	(0·01)	(0·01)	(0·00)	(0·02)			
AK-98	1425	5	melt	92	48·28	1·88	10·09	14·02	0·14	12·82	8·71	2·14	0·76	0·00	0·22	0·11	99·19	62	
					(0·19)	(0·04)	(0·42)	(0·13)	(0·04)	(0·20)	(0·12)	(0·08)	(0·03)	(0·01)	(0·01)	(0·03)			
	1425	2	ol	8	40·13	0·04	0·10	15·82	0·09	44·05	0·30	0·04	0·01	0·00	0·00	0·07	100·66	83	0·33
					(0·20)	(0·00)	(0·02)	(0·06)	(0·03)	(0·07)	(0·04)	(0·01)	(0·01)	(0·00)	(0·00)	(0·01)			
AK-99	1400	4	melt	90	48·64	1·91	10·29	13·99	0·19	12·26	8·92	2·28	0·77	0·02	0·24	0·13	99·64	61	
					(0·11)	(0·03)	(0·26)	(0·16)	(0·04)	(0·39)	(0·34)	(0·07)	(0·01)	(0·02)	(0·02)	(0·03)			
	1400	2	ol	10	40·00	0·06	0·08	16·24	0·15	43·23	0·37	0·05	0·00	0·00	0·00	0·11	100·29	83	0·33
					(0·31)	(0·03)	(0·03)	(0·19)	(0·02)	(0·16)	(0·01)	(0·00)	(0·00)	(0·01)	(0·00)	(0·03)			
AK-100	1350	3	melt	81	48·32	2·07	10·99	14·14	0·16	10·52	9·41	2·45	0·82	0·02	0·26	0·08	99·23	57	
					(0·17)	(0·01)	(0·12)	(0·04)	(0·06)	(0·05)	(0·09)	(0·04)	(0·02)	(0·02)	(0·02)	(0·01)			
	1350	4	ol	12	39·63	0·05	0·11	17·50	0·17	42·30	0·35	0·04	0·01	0·05	0·00	0·08	100·28	81	0·31
					(0·04)	(0·02)	(0·02)	(0·20)	(0·05)	(0·39)	(0·04)	(0·02)	(0·01)	(0·05)	(0·01)	(0·03)			
	1350	2	cpx	6	54·22	0·29	3·17	9·69	0·20	24·77	6·36	0·37	0·01	0·02	0·00	0·38	99·47	82	0·29
					(0·35)	(0·04)	(0·02)	(0·28)	(0·04)	(0·62)	(0·39)	(0·02)	(0·02)	(0·02)	(0·00)	(0·05)			
AK-101	1300	4	melt	51	47·54	2·73	13·94	15·21	0·19	6·58	8·05	3·81	1·40	0·02	0·36	0·02	99·83	44	
					(0·53)	(0·08)	(0·62)	(0·91)	(0·06)	(0·53)	(0·56)	(0·47)	(0·21)	(0·02)	(0·04)	(0·03)			
	1300	4	ol	14	38·95	0·06	0·08	21·85	0·17	38·92	0·33	0·05	0·02	0·06	0·00	0·05	100·54	76	0·24
					(0·21)	(0·02)	(0·03)	(0·19)	(0·04)	(0·67)	(0·01)	(0·03)	(0·01)	(0·03)	(0·00)	(0·02)			
	1300	3	cpx	35	52·33	0·59	4·82	9·62	0·18	19·24	11·40	0·64	0·02	0·07	0·04	0·28	99·22	78	0·22
					(0·34)	(0·11)	(0·33)	(0·17)	(0·03)	(0·34)	(0·76)	(0·09)	(0·01)	(0·02)	(0·02)	(0·05)			
P-518	1275	1	melt	36	46·06	3·30	15·48	16·18	0·03	5·83	6·63	4·50	1·90	0·00	0·51	0·06	100·48	39	
	1275	6	ol	8	39·14	0·09	0·02	25·03	0·24	36·71	0·31	0·03	0·00	0·01	0·01	0·03	101·62	72	0·25
					(0·23)	(0·03)	(0·02)	(0·17)	(0·08)	(0·28)	(0·04)	(0·03)	(0·01)	(0·01)	(0·01)	(0·02)			
	1275	2	cpx	56	51·15	0·85	7·83	11·56	0·14	17·41	10·43	0·94	0·04	0·02	0·04	0·18	100·58	73	0·24
					(0·17)	(0·10)	(0·45)	(0·07)	(0·02)	(0·29)	(0·52)	(0·04)	(0·06)	(0·01)	(0·00)	(0·01)			
P-519	1250	5	melt	35	48·51	3·32	16·6	14·91	0·11	4·41	6·16	4·19	1·91	0·01	0·51	0·01	100·67	35	
					(0·27)	(0·12)	(0·31)	(0·30)	(0·07)	(0·55)	(0·44)	(0·17)	(0·16)	(0·02)	(0·04)	(0·01)			
	1250	5	ol	7	38·68	0·04	0·08	26·04	0·24	35·80	0·28	0·04	0·02	0·02	0·00	0·03	101·27	71	0·22
					(0·65)	(0·03)	(0·02)	(0·28)	(0·06)	(0·36)	(0·07)	(0·01)	(0·01)	(0·03)	(0·00)	(0·03)			
	1250	5	cpx	69	51·63	1·15	7·01	10·55	0·16	16·37	12·70	0·94	0·01	0·05	0·03	0·26	100·86	73	0·19
					(0·14)	(0·04)	(0·12)	(0·19)	(0·06)	(0·38)	(0·54)	(0·04)	(0·01)	(0·03)	(0·02)	(0·05)			

Run no.	T (°C)	n[1]	Phase[2]		SiO_2	TiO_2	Al_2O_3	FeO*	MnO	MgO	CaO	Na_2O	K_2O	NiO	P_2O_5	Cr_2O_3	Total	Mg-no.[3]	K_D[4]
2 GPa																			
P-516	1500	11	melt	100	49·53	1·73	9·64	13·24	0·19	16·23	8·07	2·10	0·71	0·03	0·20	0·11	101·78	69	
					(0·31)	(0·06)	(0·09)	(0·21)	(0·05)	(0·23)	(0·08)	(0·06)	(0·02)	(0·03)	(0·03)	(0·02)			
P-515	1475	10	melt	98	47·98	1·72	9·45	13·42	0·15	15·74	8·16	1·95	0·66	0·01	0·18	0·12	99·55	68	
					(0·21)	(0·05)	(0·12)	(0·22)	(0·05)	(0·17)	(0·09)	(0·04)	(0·03)	(0·01)	(0·02)	(0·03)			
P-514	1450	10	melt	85	47·43	2·01	10·70	13·40	0·14	13·48	9·14	2·29	0·80	0·01	0·23	0·08	99·71	64	
					(0·30)	(0·07)	(0·14)	(0·10)	(0·07)	(0·12)	(0·10)	(0·06)	(0·03)	(0·01)	(0·02)	(0·02)			
P-513	1400	5	melt	66	46·09	2·33	11·46	14·93	0·17	11·55	8·42	3·27	1·03	0·04	0·28	0·08	99·66	58	
					(0·53)	(0·07)	(0·23)	(0·46)	(0·09)	(0·52)	(0·11)	(1·22)	(0·15)	(0·04)	(0·03)	(0·02)			
	1400	1	ol	2	39·36	0·05	0·11	18·34	0·23	41·82	0·36	0·02	0·00	0·00	0·00	0·05	100·35	80	0·34
	1400	2	cpx	31	53·75	0·31	4·78	9·43	0·18	22·35	8·25	0·69	0·01	0·02	0·01	0·26	100·03	81	0·33
					(0·24)	(0·02)	(0·00)	(0·24)	(0·05)	(0·65)	(0·03)	(0·02)	(0·01)	(0·00)	(0·01)	(0·04)			
AK-103	1350	2	melt	53	44·91	3·17	12·50	16·07	0·21	10·35	9·35	2·15	0·80	0·00	0·25	0·05	99·80	53	
					(1·34)	(0·41)	(0·43)	(4·22)	(0·12)	(2·18)	(2·91)	(1·00)	(0·79)	(0·00)	(0·06)	(0·07)			
	1350	2	ol	5	39·04	0·09	0·13	21·74	0·12	39·11	0·33	0·03	0·01	0·05	0·00	0·04	100·68	76	0·36
					(0·39)	(0·01)	(0·03)	(0·15)	(0·09)	(0·06)	(0·05)	(0·00)	(0·02)	(0·04)	(0·00)	(0·05)			
	1350	9	cpx	43	52·37	0·63	6·28	10·36	0·17	19·47	9·78	0·92	0·02	0·06	0·02	0·24	100·31	77	0·34
					(0·39)	(0·12)	(0·53)	(0·60)	(0·05)	(0·78)	(1·15)	(0·06)	(0·02)	(0·02)	(0·02)	(0·03)			
AK-102	1300	1	melt	26	43·45	2·52	11·90	19·62	0·16	10·68	2·84	3·93	2·68	0·00	0·45	0·04	98·29	49	
	1300	4	ol	7	38·93	0·08	0·10	22·44	0·17	37·78	0·32	0·04	0·01	0·01	0·00	0·03	99·89	75	0·32
					(0·36)	(0·04)	(0·01)	(0·42)	(0·08)	(0·61)	(0·04)	(0·04)	(0·01)	(0·02)	(0·00)	(0·03)			
	1300	8	cpx	69	51·49	0·69	7·21	10·49	0·17	18·38	9·90	1·02	0·03	0·04	0·02	0·25	99·68	76	0·31
					(0·22)	(0·07)	(0·49)	(0·32)	(0·04)	(0·53)	(0·54)	(0·06)	(0·03)	(0·04)	(0·03)	(0·06)			
2·5 GPa																			
P-531	1475	2	melt	n.d.	46·00	2·43	11·52	16·59	0·21	13·13	8·21	1·90	0·68	0·00	0·33	0·09	101·08	59	
					(0·64)	(0·01)	(0·09)	(0·07)	(0·07)	(0·85)	(0·19)	(0·87)	(0·54)	(0·00)	(0·00)	(0·01)			
	1475	7	cpx	n.d.	54·68	0·35	5·66	9·40	0·17	21·79	7·83	0·80	0·01	0·02	0·01	0·23	100·93	81	0·34
					(0·46)	(0·03)	(0·30)	(0·20)	(0·05)	(0·38)	(0·47)	(0·08)	(0·01)	(0·02)	(0·01)	(0·04)			
P-530	1450	1	melt	n.d.	44·76	3·39	14·35	14·29	0·21	8·62	11·19	1·97	0·08	0·02	0·19	0·06	99·10	52	
	1450	7	cpx	n.d.	53·77	0·42	6·72	9·57	0·16	20·04	8·99	0·98	0·02	0·02	0·02	0·20	100·91	79	0·29
					(0·29)	(0·06)	(0·42)	(0·17)	(0·05)	(0·44)	(0·33)	(0·04)	(0·02)	(0·02)	(0·03)	(0·03)			
	1450	6	ol	n.d.	40·49	0·04	0·19	19·34	0·18	41·14	0·37	0·04	0·01	0·02	0·00	0·03	101·85	79	0·28
					(0·12)	(0·01)	(0·08)	(0·29)	(0·03)	(0·31)	(0·08)	(0·01)	(0·01)	(0·03)	(0·00)	(0·02)			

Table 3: continued

Run no.	T (°C)	n^1	Phase[2]		SiO_2	TiO_2	Al_2O_3	FeO*	MnO	MgO	CaO	Na_2O	K_2O	NiO	P_2O_5	Cr_2O_3	Total	Mg-no.[3]	K_D[4]
3 GPa																			
P-509	1550	5	melt	100	49·20	1·77	9·60	10·60	0·20	16·20	8·09	1·81	0·59	0·01	0·19	0·11	98·38	73	
					(0·36)	(0·03)	(0·07)	(0·27)	(0·03)	(0·48)	(0·26)	(0·14)	(0·29)	(0·02)	(0·02)	(0·03)			
P-510	1525	5	melt	80	46·77	2·16	10·06	15·09	0·19	13·98	8·34	1·63	0·45	0·01	0·28	0·10	99·06	62	
					(0·92)	(0·46)	(0·72)	(0·74)	(0·02)	(0·81)	(0·93)	(0·45)	(0·42)	(0·01)	(0·02)	(0·02)			
	1525	4	cpx	20	53·15	0·29	5·93	8·22	0·10	21·16	8·64	1·02	0·01	0·01	0·20	0·21	98·95	82	0·36
					(0·78)	(0·03)	(0·48)	(0·28)	(0·04)	(0·84)	(0·50)	(0·06)	(0·01)	(0·01)	(0·02)	(0·05)			
P-507	1500	3	melt	70	39·54	4·06	11·81	20·43	0·17	11·20	8·53	1·93	0·29	0·00	0·17	0·05	98·18	49	
					(4·16)	(1·49)	(1·51)	(6·62)	(0·06)	(0·85)	(1·66)	(0·38)	(0·29)	(0·00)	(0·06)	(0·02)			
	1500	5	cpx	30	52·98	0·35	6·30	8·85	0·14	20·15	8·80	1·20	0·02	0·02	0·09	0·19	99·09	80	0·24
					(0·50)	(0·04)	(0·23)	(0·17)	(0·03)	(0·76)	(0·48)	(0·08)	(0·01)	(0·02)	(0·08)	(0·02)			
P-511	1475	12	cpx	73	53·26	0·41	6·29	9·27	0·15	19·89	9·20	1·34	0·01	0·01	0·02	0·16	100·01	79	
					(0·43)	(0·04)	(0·23)	(0·25)	(0·05)	(0·57)	(0·56)	(0·07)	(0·01)	(0·01)	(0·01)	(0·03)			
	1475	2	grt	8	42·21	0·76	22·86	11·59	0·23	18·25	4·78	0·05	0·00	0·00	0·01	0·35	101·08	74	
					(0·09)	(0·04)	(0·19)	(0·39)	(0·00)	(0·35)	(0·17)	(0·03)	(0·01)	(0·00)	(0·01)	(0·07)			
P-512	1450	6	cpx	65	52·74	0·62	6·44	9·77	0·15	17·49	10·42	1·70	0·03	0·01	0·02	0·16	99·55	76	
					(0·46)	(0·03)	(0·09)	(0·15)	(0·05)	(0·20)	(0·44)	(0·04)	(0·02)	(0·01)	(0·01)	(0·01)			
	1450	2	grt	19	41·82	0·91	22·70	13·22	0·23	16·95	5·17	0·06	0·01	0·01	0·05	0·24	101·35	70	
					(0·11)	(0·08)	(0·08)	(0·42)	(0·02)	(0·26)	(0·12)	(0·03)	(0·01)	(0·01)	(0·01)	(0·01)			
	1450	2	ol	6	38·34	0·05	0·16	23·55	0·12	37·44	0·31	0·06	0·02	0·00	0·00	0·02	100·07	74	
					(0·17)	(0·00)	(0·01)	(0·06)	(0·05)	(0·02)	(0·01)	(0·02)	(0·02)	(0·00)	(0·00)	(0·01)			
P-508	1400	7	cpx	54	52·68	0·63	6·38	9·83	0·15	17·32	10·67	1·80	0·03	0·02	0·03	0·15	99·69	76	
					(0·47)	(0·04)	(0·04)	(0·10)	(0·07)	(0·11)	(0·16)	(0·06)	(0·01)	(0·02)	(0·02)	(0·03)			
	1400	5	grt	26	41·34	1·21	22·12	13·81	0·26	16·06	5·49	0·12	0·02	0·00	0·08	0·19	100·70	67	
					(0·45)	(0·23)	(0·37)	(0·29)	(0·03)	(0·24)	(0·23)	(0·03)	(0·01)	(0·01)	(0·03)	(0·02)			
	1400	3	ol	13	38·59	0·05	0·16	23·40	0·19	37·24	0·32	0·07	0·01	0·00	0·00	0·03	100·06	74	
					(0·35)	(0·02)	(0·01)	(0·20)	(0·01)	(0·36)	(0·01)	(0·03)	(0·01)	(0·00)	(0·00)	(0·02)			
P-529	1525	7	cpx	n.d.	51·85	0·61	6·53	10·03	0·12	17·70	10·38	1·78	0·01	0·02		0·12	99·14	76	
					(0·12)	(0·13)	(0·27)	(0·22)	(0·02)	(0·89)	(0·69)	(0·16)	(0·01)	(0·03)		(0·04)			
	−1425	3	grt	n.d.	40·64	0·86	22·67	13·14	0·18	17·32	4·87	0·06	0·01	0·01		0·24	100·00	70	
					(0·09)	(0·20)	(0·21)	(0·76)	(0·01)	(0·12)	(0·24)	(0·02)	(0·02)	(0·01)		(0·09)			
		3	ol	n.d.	37·49	0·07	0·13	26·02	0·13	36·43	0·28	0·06	0·01	0·01		0·02	100·65	71	
					(0·20)	(0·01)	(0·01)	(0·18)	(0·00)	(0·25)	(0·03)	(0·02)	(0·01)	(0·02)		(0·04)			

Run no.	T (°C)	n[1]	Phase[2]		SiO_2	TiO_2	Al_2O_3	FeO*	MnO	MgO	CaO	Na_2O	K_2O	NiO	P_2O_5	Cr_2O_3	Total	Mg-no.[3]	K_D[4]
5 GPa																			
S-1317	1650	4	melt	100	49·10	1·73	9·58	12·46	0·17	16·11	7·92	2·04	0·71	0·01	0·21	0·11	100·15	70	
					(0·28)	(0·04)	(0·09)	(0·12)	(0·06)	(0·06)	(0·07)	(0·06)	(0·01)	(0·01)	(0·02)	(0·02)			
S-1300	1600	6	melt	30	49·82	1·90	7·99	12·46	0·12	15·88	9·02	1·73	0·14	0·01		0·13	99·20	69	
					(0·20)	(0·15)	(0·33)	(0·46)	(0·02)	(0·56)	(0·70)	(0·14)	(0·11)	(0·02)		(0·04)			
/S-1314	1600	12	grt	17	42·18	1·01	22·50	11·80	0·20	17·75	4·77	0·10	0·01	0·02	0·03	0·25	100·61	73	
					(0·31)	(0·19)	(0·44)	(0·28)	(0·05)	(0·45)	(0·38)	(0·03)	(0·01)	(0·03)	(0·01)	(0·07)			
	1600	17	cpx	57	54·40	0·45	5·58	8·51	0·11	18·40	10·00	1·91	0·04	0·01	0·02	0·15	99·58	79	
					(0·32)	(0·05)	(0·28)	(0·16)	(0·05)	(0·27)	(0·41)	(0·09)	(0·01)	(0·01)	(0·02)	(0·03)			
S-1308	1550	2	grt	22	42·38	1·30	20·52	10·87	0·22	17·74	5·21	0·24	0·03	0·03	0·05	0·71	99·30	74	
					(0·34)	(0·18)	(0·03)	(0·02)	(0·04)	(0·20)	(0·05)	(0·08)	(0·01)	(0·01)	(0·00)	(0·02)			
	1550	4	cpx	62	53·99	0·73	5·55	7·40	0·14	17·38	10·11	2·15	0·05	0·06	0·01	0·37	97·92	81	
					(0·65)	(0·07)	(0·11)	(0·39)	(0·04)	(0·45)	(0·25)	(0·11)	(0·01)	(0·02)	(0·01)	(0·15)			
S-1295	1500	1	melt	10	51·53	1·22	8·26	11·82	0·18	16·11	8·63	2·04	0·08	0·01	0·11	0·13	100·10	71	
/S-1315	1500	3	grt	16	42·14	1·15	22·16	12·45	0·24	17·72	4·74	0·16	0·05	0·00	0·11	0·31	101·24	72	0·96
					(0·60)	(0·16)	(0·16)	(0·01)	(0·03)	(0·08)	(0·45)	(0·03)	(0·04)	(0·00)	(0·03)	(0·18)			
	1500	8	cpx	69	55·27	0·53	4·70	8·48	0·12	18·22	10·73	1·92	0·03	0·02	0·03	0·15	100·20	79	0·63
					(0·20)	(0·08)	(0·22)	(0·41)	(0·04)	(0·46)	(0·51)	(0·08)	(0·02)	(0·02)	(0·03)	(0·05)			
S-1318	1450	3	melt	5	51·47	0·87	8·72	11·20	0·13	16·36	9·25	1·99	0·12	0·01	0·24	0·14	100·49	72	
					(1·05)	(0·02)	(1·11)	(0·62)	(0·05)	(0·11)	(0·22)	(0·32)	(0·05)	(0·02)	(0·31)	(0·02)			
	1450	3	grt	18	41·92	1·92	20·51	15·81	0·27	15·86	4·82	0·30	0·12	0·01	0·12	0·15	101·82	64	1·46
					(1·20)	(0·65)	(0·84)	(0·80)	(0·07)	(0·44)	(0·40)	(0·12)	(0·17)	(0·01)	(0·07)	(0·05)			
	1450	2	cpx	63	54·62	0·81	4·65	9·64	0·11	16·11	12·03	2·38	0·06	0·00	0·03	0·11	100·55	75	0·87
					(0·12)	(0·08)	(0·21)	(0·14)	(0·06)	(0·82)	(0·04)	(0·02)	(0·02)	(0·00)	(0·02)	(0·04)			
	1450	2	ol	5	46·38	0·33	1·52	20·45	0·18	31·60	3·16	1·01	0·04	0·00	0·02	0·03	104·71	73	0·95
					(4·25)	(0·05)	(0·47)	(2·37)	(0·11)	(2·08)	(0·42)	(0·57)	(0·00)	(0·00)	(0·02)	(0·05)			
S-1291	1400	3	grt	22	42·41	1·47	21·42	15·81	0·28	14·67	5·39	0·31	0·16	0·03	0·10	0·16	102·20	62	
					(0·73)	(0·20)	(0·29)	(0·21)	(0·03)	(0·66)	(0·68)	(0·18)	(0·13)	(0·03)	(0·08)	(0·02)			
	1400	2	ol	10	39·06	0·11	0·10	27·08	0·19	35·82	0·22	0·07	0·00	0·00	0·00	0·03	102·69	70	
					(0·02)	(0·03)	(0·00)	(0·23)	(0·05)	(0·05)	(0·01)	(0·01)	(0·01)	(0·01)	(0·00)	(0·01)			
	1400	5	cpx	65	55·01	0·97	5·47	9·87	0·13	15·99	10·20	2·51	0·06	0·01	0·03	0·15	100·41	74	
					(0·19)	(0·32)	(0·07)	(0·26)	(0·03)	(0·12)	(0·38)	(0·13)	(0·01)	(0·03)	(0·01)	(0·02)			

Table 3: continued

Run no.	T (°C)	n^1	Phase[2]		SiO_2	TiO_2	Al_2O_3	FeO*	MnO	MgO	CaO	Na_2O	K_2O	NiO	P_2O_5	Cr_2O_3	Total	Mg-no.[3]	K_D[4]
7GPa																			
S-1330	1750	3	melt	95	48·43	2·49	7·09	15·97	0·16	14·18	8·83	2·26	0·44	0·02	0·16	0·08	100·12	61	
					(1·09)	(0·69)	(0·29)	(1·27)	(0·10)	(0·59)	(0·32)	(0·15)	(0·20)	(0·03)	(0·07)	(0·02)			
	1750	4	grt	1	44·26	0·72	21·55	10·32	0·20	19·02	5·19	0·16	0·01	0·00	0·03	0·29	101·75	77	0·48
					(0·32)	(0·20)	(0·36)	(0·15)	(0·09)	(0·18)	(0·13)	(0·03)	(0·01)	(0·01)	(0·03)	(0·04)			
	1750	5	cpx	4	56·39	0·28	5·69	6·81	0·06	17·33	11·40	2·30	0·06	0·02	0·03	0·15	100·52	82	0·35
					(0·38)	(0·05)	(0·31)	(0·14)	(0·04)	(0·26)	(0·43)	(0·07)	(0·02)	(0·02)	(0·03)	(0·02)			
S-1319	1700	12	cpx	n.d.	55·52	0·47	5·02	8·38	0·11	17·48	11·26	2·40	0·08	0·01	0·04	0·13	100·88	79	
					(0·40)	(0·08)	(0·36)	(0·32)	(0·06)	(0·25)	(0·29)	(0·09)	(0·03)	(0·01)	(0·02)	(0·02)			
S-1320	1650	5	grt	60	43·10	1·22	21·25	13·54	0·23	16·79	5·04	0·18	0·01	0·02	0·10	0·23	101·72	69	
					(0·46)	(0·19)	(0·63)	(0·56)	(0·07)	(0·46)	(0·24)	(0·02)	(0·02)	(0·04)	(0·03)	(0·03)			
	1650	6	cpx	20	55·62	0·48	4·97	8·89	0·11	16·81	10·84	2·36	0·08	0·00	0·02	0·10	100·28	77	
					(0·59)	(0·07)	(0·47)	(0·58)	(0·04)	(0·15)	(0·44)	(0·09)	(0·02)	(0·01)	(0·02)	(0·03)			
S-1323	1600	2	grt	50	42·80	1·28	21·21	13·99	0·30	16·73	4·94	0·20	0·03	0·00	0·06	0·20	101·74	68	
					(0·58)	(0·03)	(0·41)	(0·69)	(0·05)	(0·41)	(0·12)	(0·02)	(0·01)	(0·00)	(0·01)	(0·13)			
	1600	4	cpx	30	55·75	0·59	4·92	8·88	0·11	16·58	11·33	2·39	0·11	0·00	0·06	0·13	100·85	77	
					(0·20)	(0·15)	(0·39)	(0·23)	(0·04)	(0·55)	(0·48)	(0·08)	(0·04)	(0·01)	(0·07)	(0·01)			
S-1324	1550	1	melt	20	44·83	4·75	2·23	27·22	0·23	11·80	5·07	3·95	1·33	0·04	0·94	0·00	102·40	44	
	1550	5	grt	48	42·84	1·82	20·60	15·04	0·22	15·66	5·01	0·38	0·04	0·01	0·15	0·12	101·88	65	0·42
					(0·82)	(0·62)	(0·87)	(0·24)	(0·06)	(0·46)	(0·76)	(0·05)	(0·02)	(0·01)	(0·01)	(0·07)			
	1550	7	cpx	30	55·80	0·64	4·61	9·14	0·14	15·92	11·45	2·58	0·14	0·01	0·04	0·11	100·58	76	0·25
					(0·32)	(0·16)	(0·16)	(0·20)	(0·05)	(0·41)	(0·34)	(0·20)	(0·02)	(0·01)	(0·02)	(0·02)			
	1550	1	ol	n.d.	39·14	0·09	0·15	25·04	0·23	36·19	0·27	0·11	0·02	0·00	0·00	0·00	101·25	72	0·30
S-1327	1500	4	cpx	n.d.	55·52	1·17	4·60	9·34	0·12	14·24	12·37	2·81	0·29	0·04	0·07	0·14	100·72	73	
					(0·62)	(0·08)	(1·13)	(0·23)	(0·05)	(0·54)	(1·17)	(0·32)	(0·03)	(0·04)	(0·01)	(0·05)			
	1500	1	ol	n.d.	39·02	0·15	0·13	27·28	0·22	34·45	0·30	0·12	0·01	0·10	0·00	0·00	101·78	69	
S-1328	1450	5	grt	56	42·09	2·54	19·14	16·95	0·23	14·57	5·03	0·46	0·11	0·05	0·18	0·12	101·38	60	
					(0·83)	(0·67)	(0·54)	(0·50)	(0·08)	(1·13)	(1·20)	(0·11)	(0·11)	(0·05)	(0·10)	(0·06)			
	1450	2	ol	6	38·90	0·15	0·11	27·07	0·11	34·52	0·28	0·12	0·03	0·14	0·08	0·02	101·52	69	
					(0·57)	(0·07)	(0·03)	(0·64)	(0·01)	(0·10)	(0·16)	(0·01)	(0·04)	(0·14)	(0·12)	(0·02)			
	1450	3	cpx	39	54·95	1·18	3·79	9·24	0·10	14·36	13·31	2·67	0·30	0·05	0·08	0·10	100·13	73	
					(0·31)	(0·11)	(0·33)	(0·14)	(0·08)	(0·09)	(0·75)	(0·23)	(0·02)	(0·04)	(0·03)	(0·04)			

Numbers in parentheses are one standard deviation./denotes repeat run.
[1]Number of analyses.
[2]Number refers to the modal proportion of the phase, determined by mass-balance calculations and X-ray mapped phase analysis.
[3]Mg-no. $= 100 \times [Mg/(Mg + Fe^{2+})]$.
[4]$K_D = (Fe/Mg)_{mineral}/(Fe/Mg)_{melt}$.

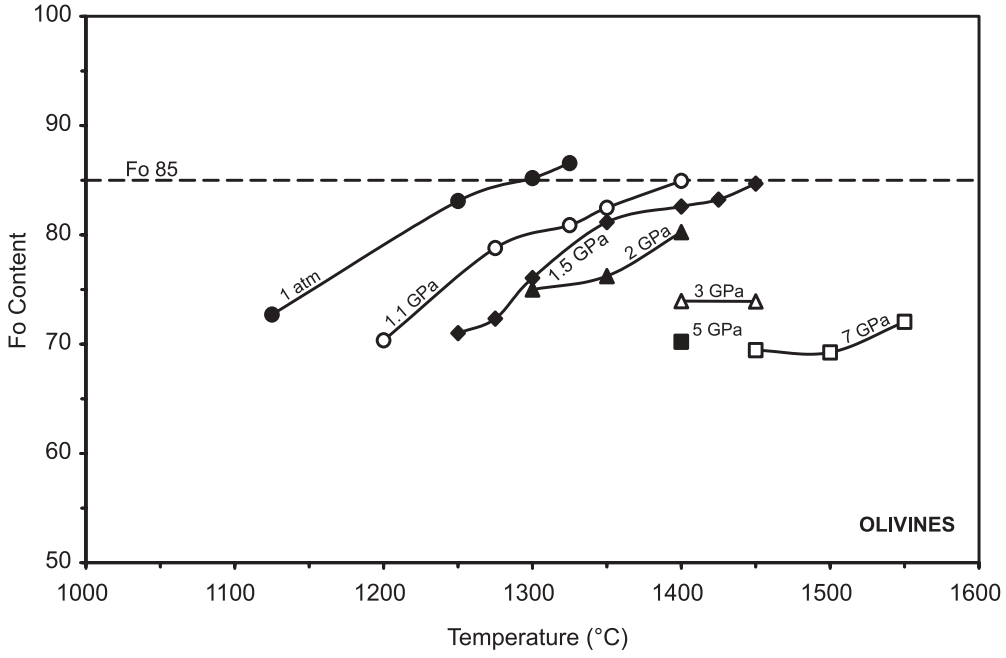

Fig. 8. Variation of forsterite content (mol %) with temperature (°C) in olivines analysed from experimental runs. The dashed line illustrates the maximum Fo content of olivine phenocrysts in 97SB68. [Note the Fo content of the reversed experimental run (see text) at 1·1 GPa and 1325°C, which follows the systematic trend of the 1·1 GPa olivines.]

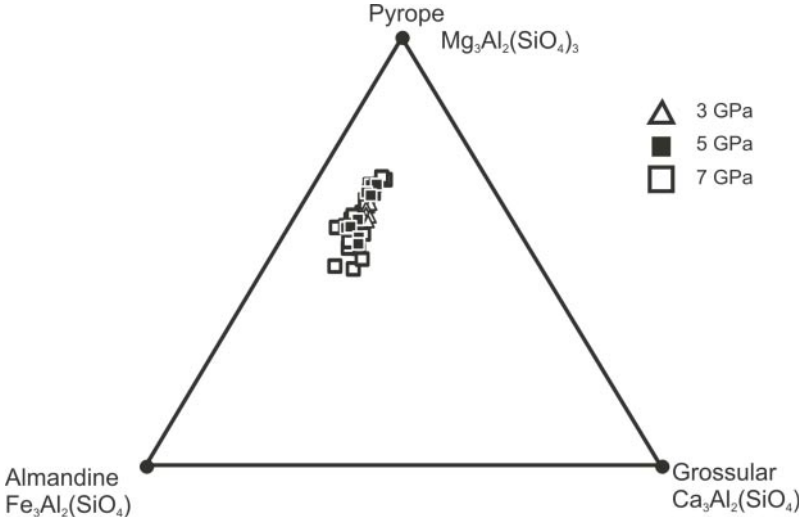

Fig. 9. Compositions of garnets analysed in 3–7 GPa runs plotted in the ternary system pyrope–almandine–grossular.

at 7 GPa for runs at 1450°C) and increase with temperature, for a given pressure. The concentration of SiO_2 in the garnets is relatively constant with pressure, but increases with temperature.

The pyroxenes are augites to sub-calcic augites (Fig. 11a) and show an increase in the jadeite component with pressure (Fig. 11b). This can be seen in the systematic marked increase in Na_2O concentration (Fig. 12) with increasing pressure (e.g. $\geq \sim$2 wt % for 5 and 7 GPa, and $\leq \sim$1 wt % for pressures of 2 GPa and lower) and decreasing temperature, at a given pressure. Pyroxenes from 1 atm runs have very similar compositions to those analysed in the original rock (Gibson *et al.*, 2000) and are likely to be relics of the powdered starting material (see above). Pyroxene K_2O contents display trends similar to those of Na_2O, with a large increase in concentration in the lowest temperature 7 GPa runs (e.g. the K_2O concentration jumps from $\sim$0·14 wt % at

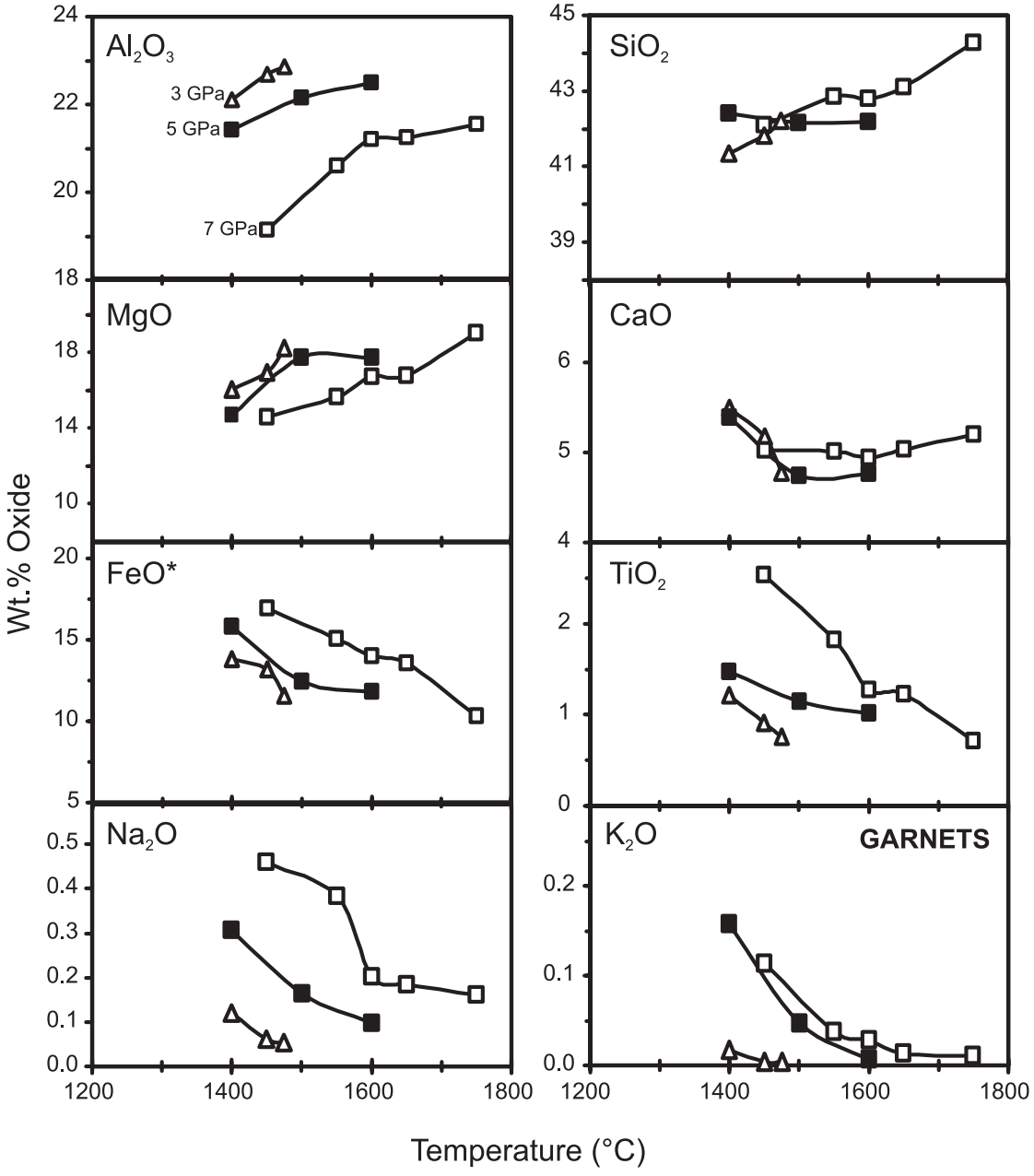

Fig. 10. Variation of major element concentrations with temperature in garnets analysed from experimental runs at 3–7 GPa.

1550°C to ~0·3 wt % at 1450°C). CaO and TiO_2 contents vary with temperature (increasing with decreasing temperature and increasing MgO content), for a given pressure. TiO_2 contents appear to increase with pressure, but CaO contents do not. In the 1 atm run at 1125°C, the high TiO_2 and CaO concentrations may reflect the presence of relic pyroxenes; however, this is based on one run and so it is difficult to know with certainty. Al_2O_3 concentrations are generally low (<9 wt %) and do not vary with pressure. Al_2O_3 concentrations of pyroxenes in runs ≤3 GPa decrease with increasing temperature, whereas those from 5 and 7 GPa runs increase in Al_2O_3 with temperature. SiO_2 concentrations increase and FeO* concentrations decrease with increasing temperature. The Mg-number of the pyroxenes increases with decreasing pressure for a given temperature; for example, from 73 at 7 GPa to 79 at 2·5 GPa at 1450°C (Table 3).

Compositions of melts

Electron microprobe analyses of melt compositions (i.e. glasses) are also reported in Table 3. Concentrations

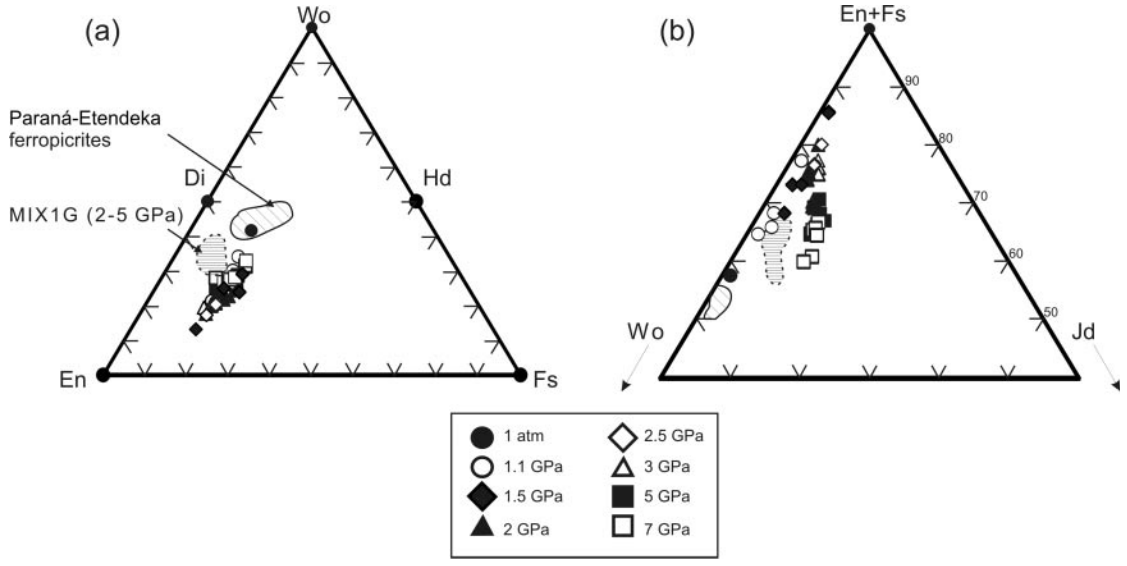

Fig. 11. Pyroxene compositions plotted in the ternary systems: (a) Wollastonite–Enstatite–Ferrosilite (Wo–En–Fs); (b) Enstatite + Ferrosilite–Wollastonite–Jadeite (En + Fs–Wo–Jd). MIX1G pyroxenes from 2–5 GPa and pyroxenes from Paraná–Etendeka ferropicrites plotted as fields for comparison. Data from Gibson *et al.* (2000), Hirschmann *et al.* (2003) and Kogiso *et al.* (2003).

of Al_2O_3, FeO*, MgO and CaO show systematic trends for experiments at all pressures (Fig. 13). The Al_2O_3 content of melts at 1 atm increases with decreasing temperature, but shows an inflection at ~13 wt % Al_2O_3, which corresponds to the onset of plagioclase crystallization (and therefore a decrease in Al_2O_3 in the melt) at 1150°C. Melt compositions between 1·1 and 2·5 GPa do not show this trend and Al_2O_3 simply increases with decreasing MgO and temperature. Al_2O_3 melt concentrations for 5 and 7 GPa experiments are relatively low (≤9 wt %) and reflect the expanded stability of garnet as the liquidus phase. CaO concentrations of experimental melts between 1 atm and 2·5 GPa increase with decreasing temperature; inflections at 1150°C (1 atm), 1300°C (1·1 GPa) and 1400°C (2 GPa) predominantly correspond to clinopyroxene crystallization. The CaO contents of melts at pressures of 3–7 GPa are relatively low and may reflect the presence of clinopyroxene throughout most of the melting–crystallization interval (and as the liquidus phase at 3 GPa). FeO* concentrations are nearly constant (~14 wt %) for pressures between 1 atm and 1·1 GPa. For pressures of 2 GPa to 7 GPa, the FeO* content decreases with increasing MgO and temperature, although 5 GPa melts show an increase in FeO* perhaps because of the nature of the quench crystals (see above). Na_2O and K_2O concentrations in the experimental melts are generally low (≤3 wt %) at 3, 5 and 7 GPa and may reflect clinopyroxene crystallization (see below).

For 1 atm to 2 GPa runs, Na_2O and K_2O concentrations in the melt decrease with increasing pressure; there is a large reduction in Na_2O concentrations for 1 atm runs from 2·15 wt % at 1275°C to 1·62 wt % at 1300°C (Fig. 13) that cannot be explained by plagioclase crystallization. A less obvious reduction is seen in K_2O concentrations at the same temperature and both trends are likely to be due to loss by volatilization in the higher temperature runs (see below).

Fe, Ni and volatile loss

The quenched melt compositions of the sample charges, above the liquidus at each pressure, exhibit a systematic loss in Fe compared with the bulk rock. A similar observation was reported by Kornprobst (1977). For pressures ≥1·1 GPa, this has been attributed to Fe alloying with the Pt container during the experimental runs. The graphite capsule promotes reducing conditions that facilitate the loss of native Fe. This Fe loss is hard to prevent because of the difficulties in controlling fO_2 within the charges. Mass-balance calculations estimate that between ~0·7 and 3 wt % of the original FeO in the bulk-starting composition was lost in experiments at ≥1·1 GPa. However, Fe loss in the graphite–Pt capsules is not significant unless the melt forms channels and connects with the Pt through the graphite; such channels were not observed here. The high estimate of Fe loss in experiments at ≥1·1 GPa may be due to large error in the modes of phases that were used to make these estimates.

In 1 atm runs, ~15% of the original FeO was lost at 1375°C as a result of alloying with the Pt wire used to suspend the charges (see above). This may be a consequence of our experimental technique, as Fe-doped Pt-wire and Re-foil were not employed here.

The Ni contents of olivine are unusually low in all experiments apart from those at 1 atm. This is unexpected, as the bulk composition contains 660 ppm Ni and should lead to high olivine Ni contents. It is possible that

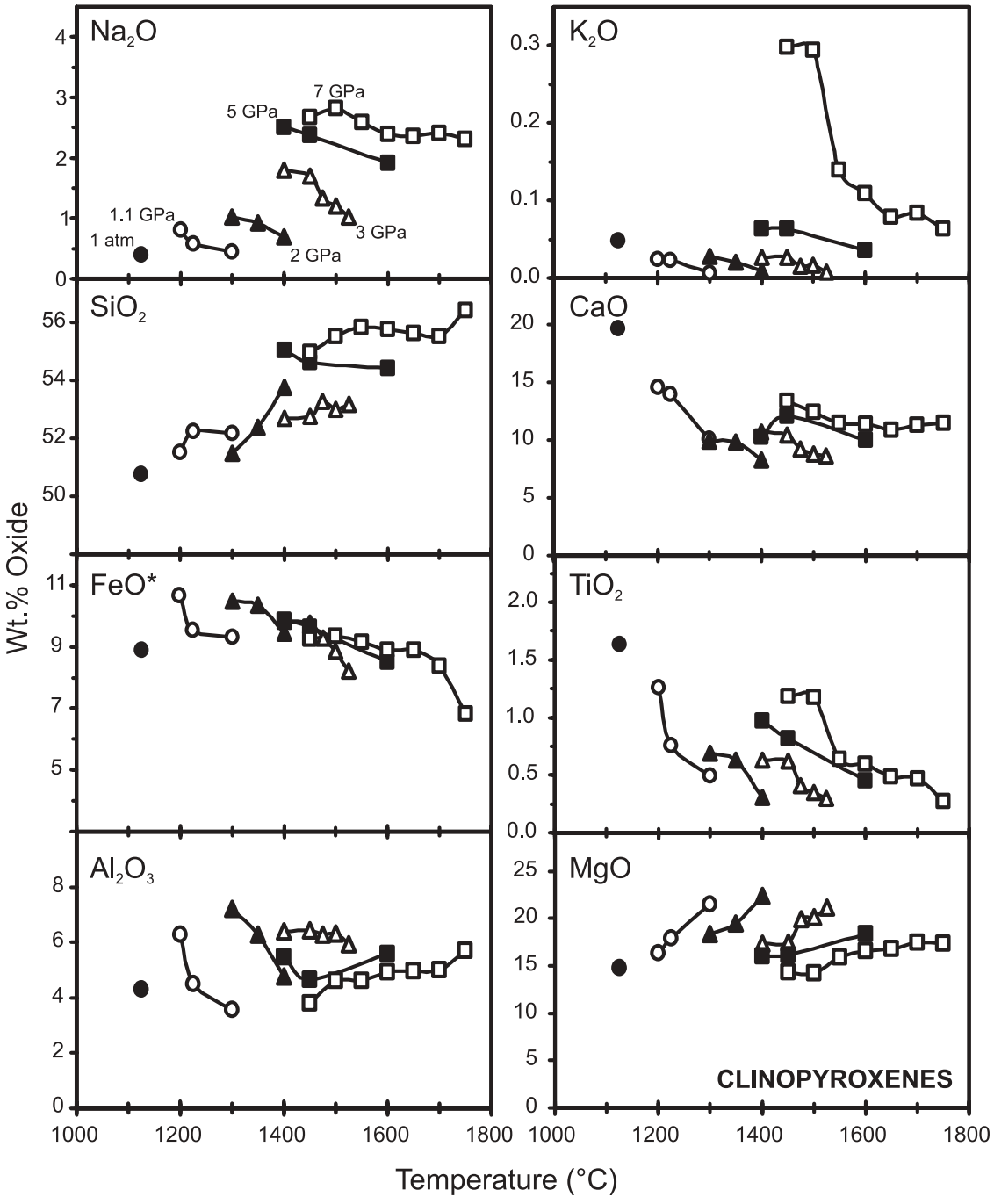

Fig. 12. Variation of major element concentrations with temperature in clinopyroxenes analysed from 1 atm to 7 GPa experimental runs.

the graphite capsules used in all of the experiments, apart from those at 1 atm, promoted conditions of Ni loss similar to the effect on Fe, although this is not well understood at present.

The charges at 1 atm also suffered from a systematic loss of volatile components, including Na_2O and K_2O. The 1 atm charges were not enclosed in capsules, and this may have permitted escape of volatile components. Loss of Na_2O and K_2O would result in the over-estimation of the positions of the olivine, plagioclase, pyroxene and solidus curves at 1 atm, as Na_2O and K_2O have the effect of lowering them (see below).

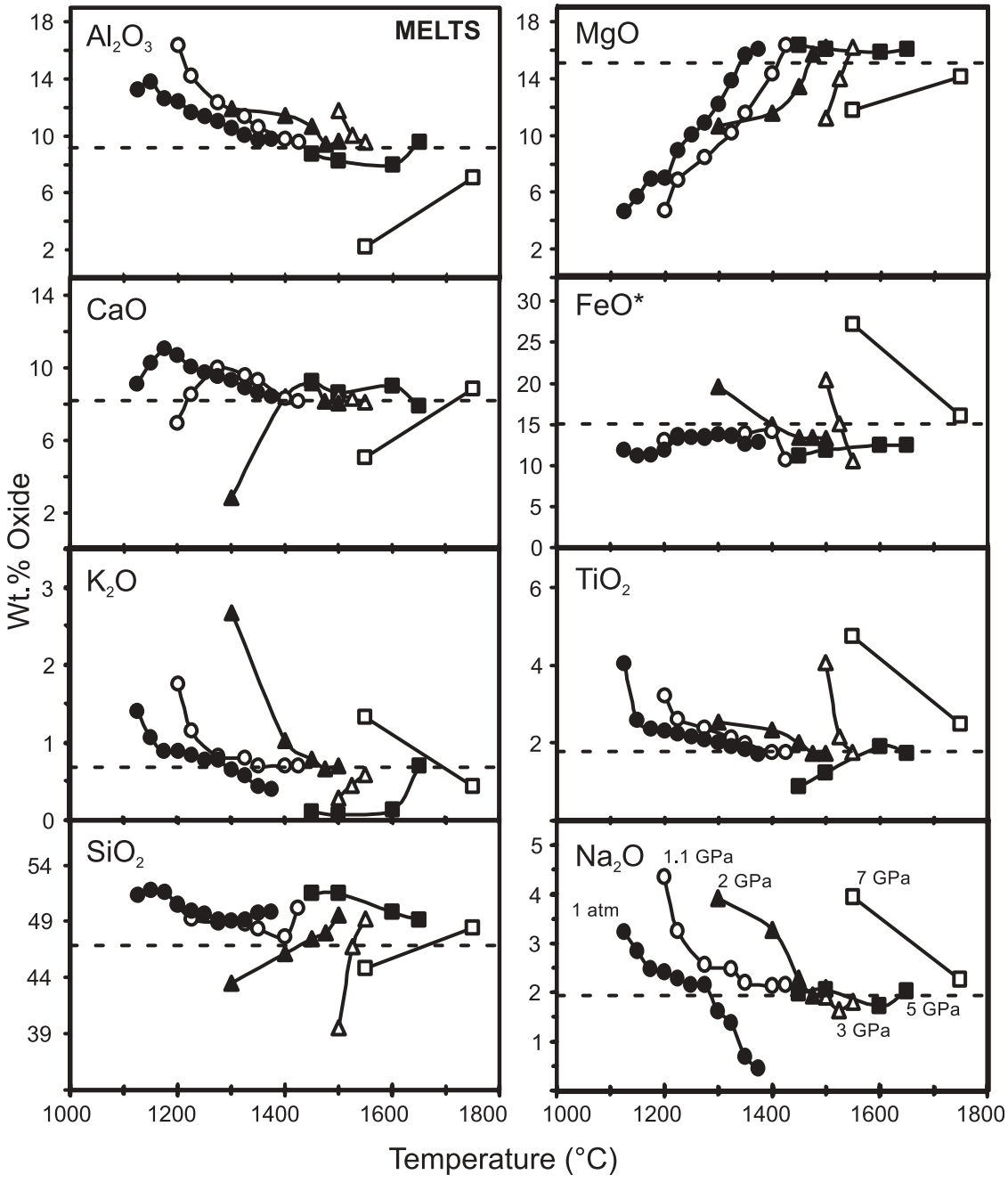

Fig. 13. Variation of major element concentrations with temperature in melts analysed from 1 atm to 7 GPa experimental runs. The bulk composition of the 97SB68 starting material is shown as a dashed line for each major element.

Inflection of the ferropicrite solidus at ~3 GPa

As shown in Fig. 4a, the solidus curve of 97SB68 has an inflection at ~3 GPa. This is in contrast to the solidus of MORB (Yasuda *et al.*, 1994) and silica-undersaturated garnet pyroxenite (e.g. MIX1G; Kogiso *et al.*, 2003; see below). The 20% melting curve for ferropicrite 97SB68 (Fig. 4b) is similar to those of experimentally determined K-poor mafic rocks (Yasuda *et al.*, 1994; Kogiso *et al.*, 2003), whereas its solidus temperatures are similar to those of K-rich alkalic basalt (Tsuruta & Takahashi, 1998) or K-doped peridotite (Wang & Takahashi, 2000). The inflection of the ferropicrite solidus may be explained by the changing effect of bulk-rock K_2O on the

solidus at different pressures (e.g. Tsuruta & Takahashi, 1998; Wang & Takahashi, 1999, 2000). According to these studies, K_2O causes a lowering of the solidus temperature at pressures above the stability field of plagioclase (the host phase of K_2O at low pressures). When plagioclase is no longer stable, the anhydrous solidus of a mafic rock is controlled by the presence or absence of K-feldspar (sanidine). The low and constant solidus temperature above 3 GPa could be due to eutectic melting in the presence of sanidine (Tsuruta & Takahashi, 1998) as a consequence of the high bulk-K_2O (0·68 wt %) content of 97SB68. Although we did not observe sanidine in our experiments, we have inferred its presence below 5 GPa from mass-balance calculations of K_2O. The clinopyroxene–garnet cotectic-like melting reported above occurs at much higher temperatures than the solidus in 97SB68, causing a low melt fraction (<20%) over a large temperature interval until the pyroxene–garnet cotectic melting temperature is reached (Fig. 5). K_2O becomes compatible in diopsidic pyroxene at pressures above ~7 GPa and its effect on the solidus diminishes (see the solidus curve of K-rich basalt; Tsuruta & Takahashi, 1998; Wang & Takahashi, 1999).

DISCUSSION

From the results of our study it is possible to place constraints on the petrogenesis of the Paraná–Etendeka ferropicrites. In the following discussion, our results are compared with those of previous experimental studies to constrain the magma generation and differentiation processes that were operating during the early development of the Paraná–Etendeka CFB. The geological implications of ferropicrite magma genesis in both continental and oceanic settings are then considered.

Comparisons with previous experimental studies of high-MgO magmas

As suggested above, the ferropicrite investigated in this study is believed to have experienced little modification by crystal fractionation or accumulation en route to the surface from its source. The rapid increase of the 97SB68 melt fraction over a relatively small temperature interval (Figs 4b and 5) also suggests that it may be appropriate to treat ferropicrite melting as having equilibrium characteristics. The generation of anhydrous primary picritic melts is widely believed to require partial melting of a peridotite mantle source at high temperatures (e.g. Green & Ringwood, 1967; Kushiro, 1969; Jaques & Green, 1980; Herzberg, 1995). Once generated, the primary melts will maintain equilibrium with the surrounding mantle until they pool and reach a segregation point. For picrites and komatiites, this point represents the shallowest depth at which the magma is in equilibrium with peridotite, such that the melt composition lies on the olivine–orthopyroxene phase boundary (Kushiro, 1969).

Komatiites

High-pressure experimental data on picrite starting materials are rare compared with those on peridotites, and comparison with previous studies is limited. We have, therefore, included a comparison of the phase relations from experiments on natural komatiite starting materials, at pressures up to 12 GPa, in Fig. 14a. The experiments of Wei *et al.* (1990) on an aluminium-depleted Barberton komatiite (ADK) and aluminium-undepleted Munro Township komatiite (AUK) were undertaken at pressures ≥4 GPa and so we have also used the liquidus of a Belingwe aluminium undepleted komatiite (NG 7621; Bickle *et al.* 1977), for comparison at pressures ≤3 GPa. The komatiite starting materials have higher MgO contents and lower FeO*, Al_2O_3, TiO_2, Na_2O and K_2O than 97SB68 (Table 1). As a consequence, the solidi of both types of komatiite are ~200°C higher than that of 97SB68 for a given pressure. Despite this difference, the phase relations of the Barberton ADK are very similar to those of 97SB68: olivine is succeeded as the liquidus phase (at 9·6 GPa) for a short interval by pyroxene; pyroxene is then followed by garnet (at 11·6 GPa; Fig. 14a).

Important differences are apparent between the phase relations of the 97SB68 ferropicrite and the Barberton ADK of Wei *et al.* (1990). First, in the high-pressure (≥5 GPa) ferropicrite experiments, garnet and clinopyroxene were found to exhibit essentially cotectic behaviour (see above). In contrast, the garnet stability field in the ADK of Wei *et al.* (1990) rapidly increases above ~10 GPa. Second, the inflection in the 97SB68 solidus is not observed in either of the komatiite solidi, although no data exist below 4 GPa (see above; Fig. 14a). As discussed above, the inflection in the 97SB68 solidus is due to its high K_2O content (0·68 wt %), which is an order of magnitude higher than in the komatiites (<0·1 wt %; Table 1).

Picrites

The ferropicrite (97SB68) has lower MgO and Al_2O_3 and higher FeO* and K_2O contents than picritic samples used in previous experimental studies (Table 1). These experiments (Green & Ringwood, 1967; Maaløe, 2004) were conducted only up to ~3 GPa but, despite this, it is apparent that the phase relations are similar to those of 97SB68 (Fig. 14b). All have large melting intervals at low pressures (e.g. >200°C at 1 GPa) with olivine as the liquidus phase until it is succeeded by pyroxene at ~2 GPa. Both the garnet-in and pyroxene-in curves

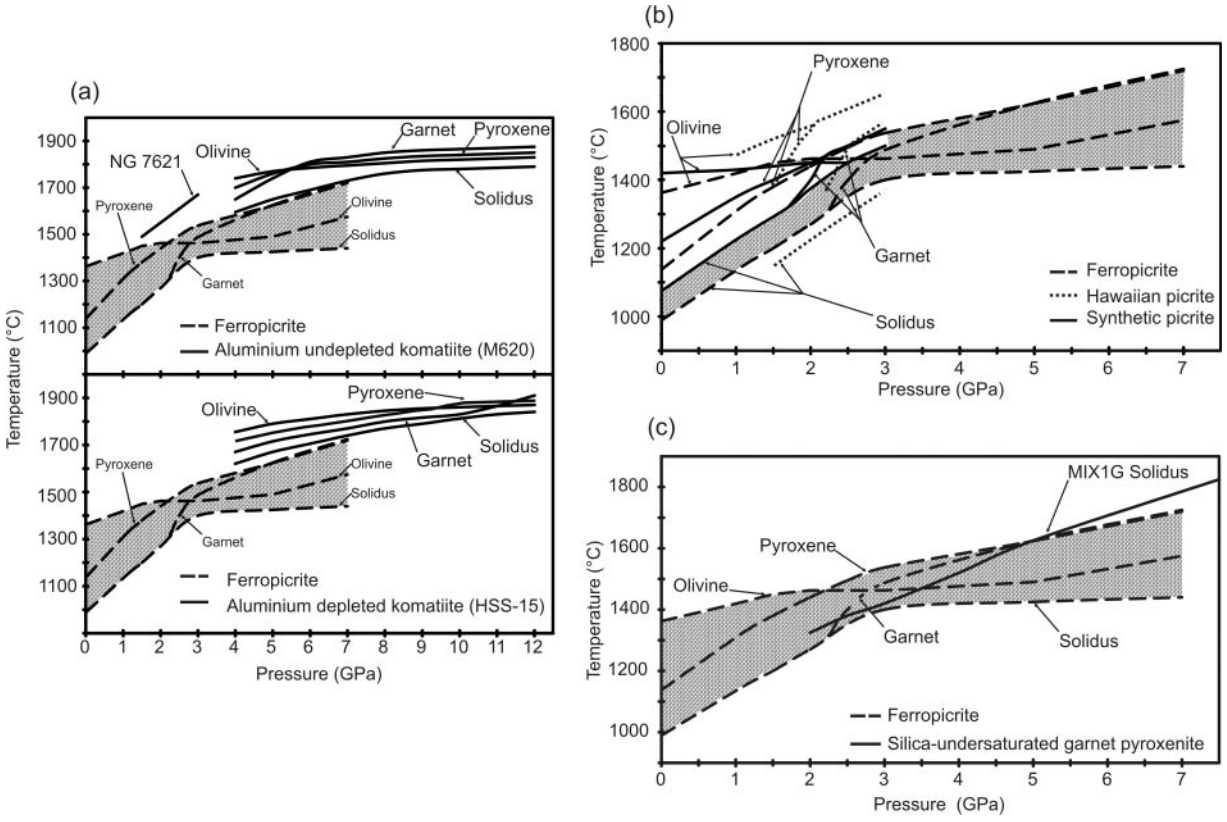

Fig. 14. Comparison of 97SB68 phase relations with: (a) aluminium-depleted komatiite and aluminium-undepleted komatiite of Wei *et al.* (1990) and Belingwe komatiite (NG 7621) liquidus of Bickle *et al.* (1977); (b) synthetic picrite of Green & Ringwood (1967) and Hawaiian picrite (183-15, with 2 wt % of $Fo_{91\cdot22}$ added) of Maaløe (2004); (c) MIX1G solidus of Kogiso *et al.* (2003). 97SB68 phase relations are shown as dashed lines and shaded, with the plagioclase liquidus of Fig. 3a omitted for clarity.

have similar dP/dT for both the picrites and 97SB68 although the garnet-in curve extends to lower pressures in the synthetic picrite. As a result, garnet succeeds pyroxene as the liquidus phase at much lower pressures in the picrite (~2·2 GPa) than the ferropicrite (~5 GPa). Both the ferropicrite and the Hawaiian picrite have pyroxene as the liquidus phase from ~2 to >3 GPa but in 97SB68 this is a clinopyroxene whereas in the picrite it is an orthopyroxene.

At pressures ≤1·25 GPa, the olivine liquidus in the ferropicrite is intermediate between the synthetic and Hawaiian picrites. Above this pressure the synthetic picrite and ferropicrite liquidi are similar, but the Hawaiian picrite liquidus is ~100°C higher. The solidus has a similar dP/dT for both the picrites and 97SB68. The synthetic picrite solidus is ~100°C higher than that of 97SB68, for a given pressure, which may in part be due to the higher bulk-rock MgO content of the starting material (Table 1), but may also be due to the different method used to constrain the solidus. We utilized X-ray compositional mapping of the run products as well as high-resolution back-scattered electron images to constrain the onset of melting (e.g. Figs 6 and 7).

Could peridotite be the ferropicrite primary melt source?

Melting studies on fertile peridotite KLB-1 have shown that olivine remains the liquidus phase at least up to 14 GPa (Takahashi & Scarfe, 1985; Takahashi, 1986; Takahashi *et al.*, 1993; Zhang & Herzberg, 1994). Below ~3·5 GPa, the most important phases in terms of volume are olivine and orthopyroxene. The behaviour of orthopyroxene at higher pressures is, however, controversial. Takahashi *et al.* (1993) observed that orthopyroxene in KLB-1 became increasingly soluble in clinopyroxene and garnet with pressure such that, above 3·5 GPa, the subsolidus assemblage was reduced to olivine, garnet and clinopyroxene. Orthopyroxene was also found by Walter (1998) to be stable in the subsolidus assemblage of garnet peridotite KR4003 up to 3·3 GPa. However, orthopyroxene was observed to crystallize from the melt at temperatures above the solidus in KR4003; this is consistent with the results of Zhang & Herzberg (1994) for KLB-1. In spite of these differences, it is clear that a primary melt derived from partial melting of a peridotite source must be in equilibrium with both olivine and pyroxene.

Table 4: Compositions (in wt %) of pyroxenites, peridotites and basalt–peridotite mixtures used in high-pressure melting experiments

	G2	MIX1G	HK66	KLB-1	KR4003	PHN-1611	GA1	MPY90	$GA1_{50}MPY90_{50}$	$GA1_{75}MPY90_{25}$
SiO_2	50·05	45·56	48·02	44·48	44·90	43·70	50·35	44·74	47·55	48·95
TiO_2	1·97	0·90	0·22	0·16	0·16	0·25	1·49	0·17	0·83	1·15
Al_2O_3	15·76	15·19	4·88	3·59	4·26	2·75	16·53	4·37	10·45	13·49
FeO*	9·35	7·77	9·90	8·10	8·02	10·05	9·83	7·55	8·70	9·27
MnO	0·17	0·15	0·14	0·12	0·13	0·13	0·17	0·11	0·14	0·16
MgO	7·90	16·67	32·35	39·22	37·30	37·22	7·94	38·57	23·26	15·61
CaO	11·74	11·48	2·97	3·44	3·45	3·26	9·60	3·38	6·49	8·05
Na_2O	3·04	1·44	0·66	0·30	0·22	0·33	3·49	0·40	1·95	2·72
K_2O	0·03	0·04	0·07	0·03	0·09	0·14	0·44	0·00	0·22	0·33
P_2O_5	—	—	—	—	—	—	0·16	0·00	0·07	0·11
NiO	—	—	—	—	—	—	0·00	0·26	0·13	0·07
Cr_2O_3	—	—	0·25	0·31	0·41	0·28	0·00	0·45	0·23	0·11
Total	100·00	99·20	99·46	99·75	98·94	98·11	100·00	100·00	100·01	100·02
Mg-no.	60	79	85	90	89	87	59	90	83	75

G2, MORB-like pyroxenite prepared from natural garnet and cpx + natural kyanite and quartz + synthetic TiO_2 (Pertermann & Hirschmann, 2003*a*, 2003*b*). MIX1G, silica-deficient garnet pyroxenite prepared from natural mineral and rock powders (Kogiso *et al.*, 2003). HK66, olivine websterite, Salt Lake Crater (Takahashi & Kushiro, 1983; Hirose & Kushiro, 1993). KLB-1, fertile spinel lherzolite, Kilborne Hole crater (Takahashi, 1986; Hirose & Kushiro, 1993; Takahashi *et al.*, 1993). KR4003, fertile garnet lherzolite, West Kettle River (Walter, 1998). PHN-1611, fertile garnet lherzolite, Thaba Putsoa (Scarfe & Takahashi, 1986; Ito & Takahashi, 1987; Kushiro, 1996). GA1, coesite eclogite crystallized from average oceanic crust (Yaxley & Green, 1998). MPY90, MORB pyrolite (Yaxley & Green, 1998). $GA1_{50}MPY90_{50}$, mixture of 50% GA1 and 50% MPY90 (Yaxley & Green, 1998). $GA1_{75}MPY90_{25}$, mixture of 75% GA1 and 25% MPY90 (Yaxley, 2000).

Constraints from 97SB68 bulk chemistry

We have used the method of O'Hara (1968) to compare the bulk-rock composition of 97SB68 with compositions of melts derived experimentally from peridotite starting materials (KLB-1, PHN-1611 and KR4003; Scarfe & Takahashi, 1986; Takahashi, 1986; Walter, 1998; Table 4). Figures 15 and 16 show the available data plotted in the pseudoternary systems forsterite–Ca-Tschermak pyroxene–quartz (Fo–CaTs–Qz) projected from diopside (Di) and garnet–forsterite–diopside (Grt–Fo–Di) projected from enstatite (En). In Fig. 15, the Paraná–Etendeka ferropicrites are distributed across the Enstatite–Ca-Tschermak thermal divide (O'Hara, 1968), although most samples (including 97SB68) plot in the silica-poor region. 97SB68 is among the most Fo normative of the Paraná–Etendeka ferropicrites and plots close to the field of 3 GPa peridotite melts. Despite this similarity in compositions it is apparent from major element variation diagrams (Fig. 17) that there are significant differences between the compositions of 97SB68 and 3 GPa peridotite partial melts; below 3·5 GPa peridotite melts are lower in FeO* and K_2O and higher in Al_2O_3 than 97SB68 at a given MgO content (Fig. 17).

Constraints from 97SB68 phase relations

If, as we propose, the composition of the ferropicrite sample investigated in our study is representative of a near primary mantle melt, its liquidus phases should also constrain the residual mineralogy and depth of separation from the source region. The phase relations of 97SB68 indicate that ferropicrite primary melt separation could have occurred at either (1) ~2·2 GPa at the olivine–clinopyroxene liquidus co-saturation point, with an olivine and clinopyroxene residue but with garnet absent; or (2) ~5 GPa at the garnet–clinopyroxene liquidus co-saturation point, with a garnet and clinopyroxene residue, but with olivine totally consumed in the melt.

The depth of ferropicrite melt separation may be further constrained from the bulk composition of the 97SB68 starting material. The low Al_2O_3 (9 wt %; Table 1) and fractionated heavy REE (HREE; e.g. $[Gd/Yb]_n = 3·1$; Gibson *et al.*, 2000) indicate that garnet was a residual phase at the time of melt separation (Table 1 and Fig. 18). We propose, therefore, that the primary melts separated from their mantle source region closer to 5 GPa rather than 2·2 GPa. The cotectic-like behaviour of garnet and clinopyroxene in 97SB68 may

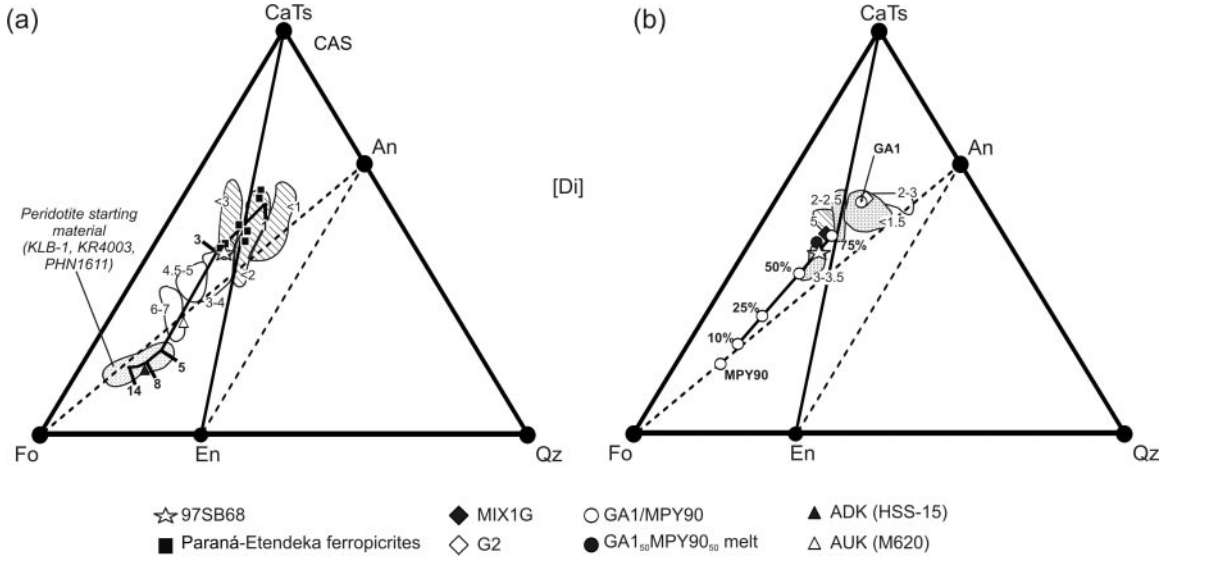

Fig. 15. Projection from diopside onto the pseudo-ternary system Mg_2SiO_4 (Fo)–$CaAl_2Si_2O_6$ (CaTs)–SiO_2 (Qz), using the method of O'Hara (1968) and modified from Kogiso *et al.* (2003). The En–CaTs join represents a thermal divide between silica-saturated and silica-undersaturated compositions. Samples plotting to the left of the Fo–An join are Ne normative, those to the right of the En–An join are Qz normative and those in between are Hy normative. (a) Peridotites: positions of KLB-1 partial melts (Takahashi, 1986; Takahashi *et al.*, 1993) are plotted as trends with pressure values indicated in bold. KR4003 melts (Walter, 1998) are shown as unfilled fields separated into pressure ranges. PHN-1611 melts (Kushiro, 1996) are shown as hatched fields and are separated into pressure intervals. Also shown are the aluminium-depleted and aluminium-undepleted komatiites of Wei *et al.* (1990). Peridotite partial melts at low pressure are silica saturated; those at ~3 GPa are close to 97SB68 in the silica-undersaturated region of the projection. (b) Pyroxenites: partial melts of G2 (unfilled field; Pertermann & Hirschmann, 2003*a*, 2003*b*), MIX1G (hatched field; Kogiso *et al.*, 2003) and HK66 (stippled fields; Takahashi & Kushiro, 1983) are shown for different pressures. Positions of GA1–MPY90 (Yaxley & Green, 1998; Yaxley, 2000) mixtures are illustrated as a trend line with the percentage of GA1 shown in bold. It must be noted that this is not a mixing line, as the En–CaTs join represents a thermal divide.

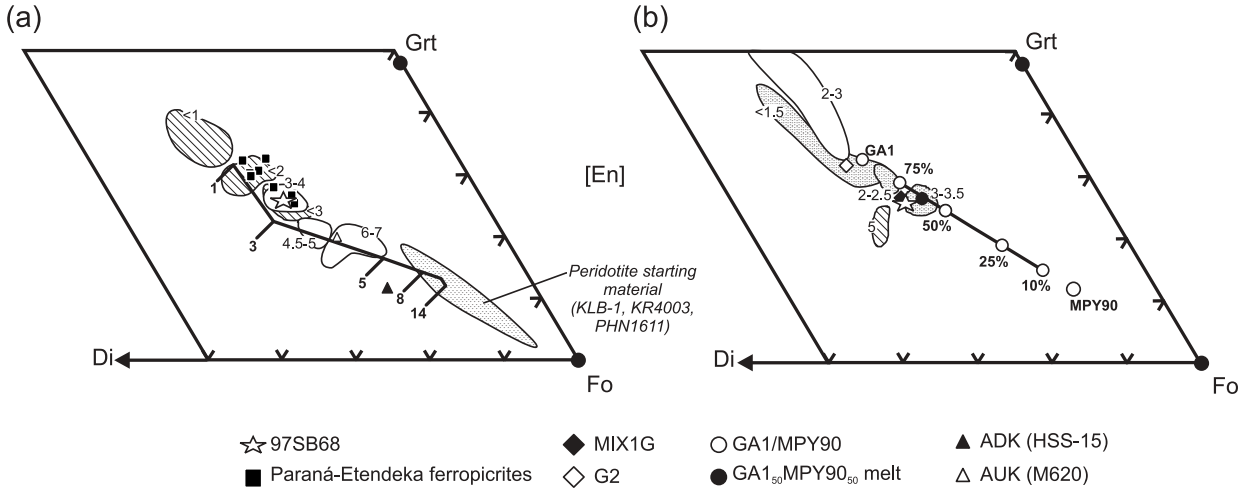

Fig. 16. Projection from enstatite onto part of the plane M_2S–C_2S_3–A_2S_3 using the method of O'Hara (1968) and modified from Wei *et al.* (1990). Data sources, fields and symbols as for Fig. 15. (a) Peridotite melts; (b) G2, MIX1G, HK66 and GA1–MPY90 melts.

indicate that the 5 GPa co-saturation point is a minimum depth of melt separation. Our findings contrast with those of Maaløe (2004), who suggested that the Hawaiian picrite separated from an olivine–orthopyroxene residue, i.e. a peridotite source. Although peridotite melt compositions are similar to 97SB68 (Figs 15a and 16a) the pressures at which they were produced are not consistent with the phase relations of 97SB68. Peridotite melts that are closest in composition to 97SB68 were formed at 3–3·5 GPa but at these pressures, the ferropicrite melt was in equilibrium only with clinopyroxene.

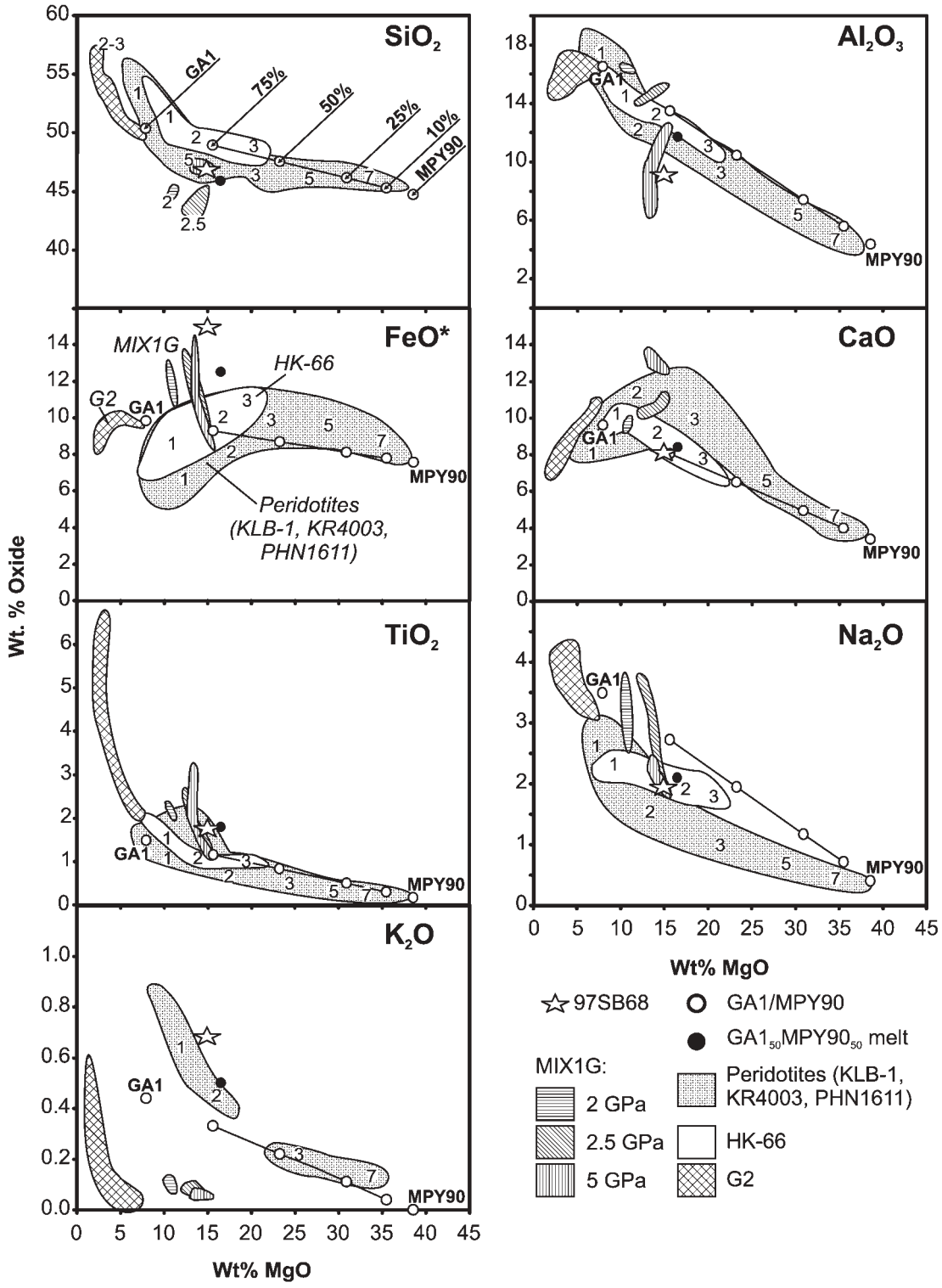

Fig. 17. Variation in concentrations of major elements against concentration of MgO for partial melts of KLB-1, KR4003, PHN-1611 and HK66, along with those of MIX1G and G2. Also shown are the compositions of basalt–peridotite (GA1–MPY90) mixtures; the percentage of GA1 is indicated in bold next to each open circle along a trend line. The composition of a picritic melt produced from $GA1_{50}MPY90_{50}$ at 3·5 GPa and the 97SB68 starting composition are also shown. Numbers indicate pressures (in GPa) of partial melting. Data are from Takahashi & Kushiro (1983), Takahashi (1986), Hirose & Kushiro (1993), Kushiro (1996), Walter (1998), Yaxley & Green (1998), Yaxley (2000), Hirschmann *et al.* (2003), Kogiso *et al.* (2003) and Pertermann & Hirschmann (2003*a*, 2003*b*).

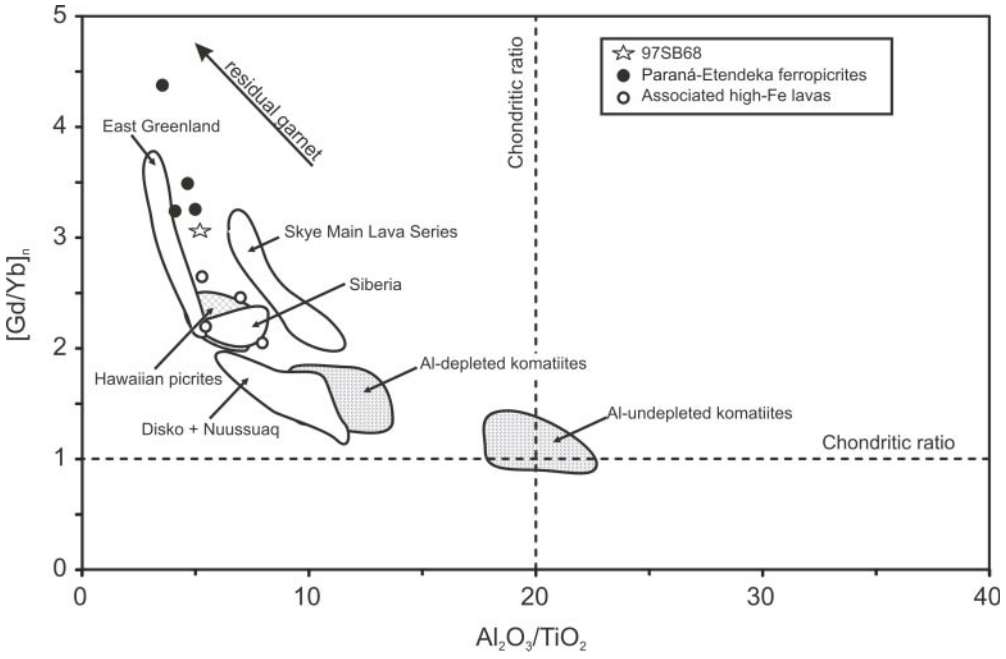

Fig. 18. Al_2O_3/TiO_2 vs $[Gd/Yb]_n$ plot, modified from Arndt (1994). 97SB68 and other Paraná–Etendeka ferropicrite data from Gibson *et al.* (2000) and Thompson *et al.* (2001). Also shown are picrites from Disko Island and Nuussuaq (West Greenland; Lightfoot *et al.*, 1997), East Greenland (Fram & Lesher, 1997), Hawaii (Norman & Garcia, 1999), the Skye Main Lava Series (Scarrow & Cox, 1995) and Siberia (Wooden *et al.*, 1993).

Garnet pyroxenite as the ferropicrite source?

The phase relations and bulk-rock composition of 97SB68 suggest that primary ferropicrite melts are unlikely to have been derived from partial melting of normal peridotite and that melting of a garnet pyroxenite source may have been significant. Recent high-pressure experimental studies have been undertaken on natural and synthetic starting materials that are thought to be similar in composition to mantle pyroxenites (we have used the term pyroxenite to include all pyroxene-dominated rocks, such as eclogite, garnet pyroxenite and websterite) and these possible ferropicrite melt source compositions are discussed below.

Olivine websterite (HK66)

HK66 (HK66101701; Kuno & Aoki, 1970) is a xenolith from the Salt Lake Crater in Hawaii. Although Kuno & Aoki (1970) described this rock as a fertile garnet lherzolite, on the basis of its modal mineralogy it should be classified as an olivine websterite. From its high FeO/MgO relative to peridotite and unusually orthopyroxene-rich nature, this rock is most likely to have formed from chemical reactions between a molten mafic component and garnet peridotite, such as experimentally demonstrated by Yaxley & Green (1998) and Takahashi & Nakajima (2002) (see below). HK66 is richer in FeO, Al_2O_3 and SiO_2 than some fertile peridotites, such as KLB-1 and KR4003 (Table 4), and this is reflected in the compositions of the partial melts (Figs 1 and 17). High-pressure melting studies of HK66 have been carried out by a number of workers (e.g. Takahashi & Kushiro, 1983; Hirose & Kushiro, 1993). According to these studies, HK66 partial melts at ~3 to 3·5 GPa are silica-undersaturated, and most are slightly more Fo-normative than 97SB68 (Fig. 15b). At ~2 to 2·5 GPa, HK66 melts plot close to the Enstatite–Ca-Tschermak join (Fig. 15b) and are silica-saturated at pressures ≤1·5 GPa. CaO and Na_2O contents of HK66 partial melts at 2 GPa are similar to those of 97SB68.

HK66 has been proposed to be similar to the mantle source region of high-Mg magmas from the Skye Main Lava Series (SMLS), NW Scotland, by Scarrow & Cox (1995). Normalized to 15 wt % MgO, the compositions of the SMLS are broadly similar to 97SB68, but the former are higher in SiO_2, Al_2O_3 and lower in FeO*. Mantle melting to produce the SMLS may have been initiated in the garnet stability field at ~3·6 GPa but the higher Al_2O_3 contents suggest that garnet may have been exhausted in the residue and that the top of the melt column resided at 1·8 GPa. This would only be the case for 97SB68 if the contributing mantle melts were generated at ≤~2·5 GPa.

Quartz eclogite (G2)

Partial melting experiments, at pressures up to 3 GPa, have recently been undertaken on a MORB-like

pyroxenite (quartz eclogite) by Pertermann & Hirschmann (2003*a*, 2003*b*). At 2–3 GPa, partial melts of quartz eclogite (G2) have higher SiO_2, Al_2O_3, Na_2O and TiO_2 and lower FeO*, MgO and K_2O than the bulk-rock composition of 97SB68 (Fig. 17). Both G2 melts and the starting material are silica-saturated (Fig. 15b) and are separated from 97SB68 by the CaTs–En thermal divide. G2 partial melts at higher pressures may become more MgO-rich and more similar in composition to 97SB68 but the G2 bulk composition should produce melts that are less olivine-normative than 97SB68. Equilibrium batch melting of subducted basaltic oceanic crust alone, therefore, could not produce a melt similar in composition to 97SB68.

Silica-undersaturated garnet pyroxenite (MIX1G)

Partial melts of a silica-undersaturated garnet pyroxenite (MIX1G; Hirschmann *et al*, 2003; Kogiso *et al.*, 2003) exhibit an increase in MgO with pressure and melts at 5 GPa plot close to the ferropicrite in Fig. 15b. Al_2O_3 concentrations decrease and SiO_2 contents increase with increasing pressure, as a result of the presence of residual garnet, such that 5 GPa melts of MIX1G are similar to 97SB68. The Na_2O concentrations of the 5 GPa melts are also similar to those of 97SB68 but all MIX1G melts have lower K_2O and FeO* and higher CaO concentrations than 97SB68 (Fig. 17), which probably reflect the composition of the starting material (Table 4). We note that the MIX1G starting material is based on a garnet pyroxenite with ~80 modal % pyroxene (Shervais & Mukasa, 1991).

Figure 14c shows a comparison of the phase relations of 97SB68 with the solidus of MIX1G (Kogiso *et al.*, 2003). The most striking difference between MIX1G and 97SB68 is in the geometry of the solidus curves. At 2 GPa the MIX1G solidus is ~50°C higher than that of 97SB68, but is only ~25°C higher at 3 GPa. Because of its high K_2O content, a marked inflection is observed in the 97SB68 solidus curve at pressures >3 GPa (see above and Fig. 4) and the MIX1G solidus is at a significantly higher temperature (e.g. ~250°C higher at 5 GPa). The inflection of the solidus at ~3 GPa results in a large melting interval for 97SB68 (e.g. ~225°C at 5 GPa, Fig. 4a and b) compared with ~100°C for MIX1G (Kogiso *et al.*, 2003). The pyroxene–garnet cotectic-like melting curve of 97SB68 is comparable with the solidus of MIX1G.

Eclogite–peridotite (GA1–MPY90)

A coesite eclogite (GA1), representative of average oceanic crust, has been used in 3·5 GPa experiments by Yaxley & Green (1998) and Yaxley (2000). They investigated the interactions between siliceous partial melts of eclogite and peridotite by sandwiching a layer of GA1 against MORB pyrolite (MPY90; Table 4). Experiments were also run on mixed compositions (i.e. GA1–MPY90; Yaxley, 2000). The starting compositions are plotted in Figs 15b and 16b. It is important to note that the trend line between the basalt (GA1) and peridotite (MPY90) does not represent a mixing curve, as the end-members are separated by the CaTs–En thermal divide. Partial melting of equal proportions of basalt and peridotite ($GA1_{50}MPY90_{50}$) at 1500°C and 3·5 GPa produces a picritic melt that is similar in composition to 97SB68 (Fig. 17). The former has slightly higher MgO (16·5 wt % compared with 14·94 wt % in 97SB68) and Al_2O_3 (11·7 wt % compared with 9·09 wt % in 97SB68), lower FeO* (12·50 wt % compared with 14·9 wt % in 97SB68) but similar K_2O contents (~0·5 wt %). Other analyses of GA1–MPY90 partial melts are not available, but low-degree melts of mixed runs containing >50% peridotite are expected to be nepheline-normative picrites (Yaxley, 2000).

If our assumption that 97SB68 is representative of the ferropicrite primary melt composition is valid then the mantle source must be more Fe-rich than $GA1_{50}MPY90_{50}$. One way of achieving this is to increase the basalt (GA1) component of the GA1–MPY90 mixture. Melt compositions of 97SB68 decrease in Al_2O_3 with increasing pressure (Fig. 13) and partial melts move towards the Fo apex in Figs 15b and 16b. It is likely that at >3·5 GPa the picritic partial melt of $GA1_{50}MPY90_{50}$ will also become more olivine normative and, therefore, move further away from the composition of 97SB68. At 3·5 GPa, a partial melt of $GA1_{75}MPY90_{25}$ would lie very close to the CaTs–En divide, just in the silica-undersaturated field. At 5 GPa, however, the partial melt composition would be more olivine normative and may be closer in composition to 97SB68. We therefore believe that a mixture of 75% basalt and 25% peridotite may yield a melt composition similar to 97SB68 at ~5 GPa. This composition probably represents the maximum amount of peridotite, as 97SB68 is one of the most magnesian of the suite of Paraná–Etendeka ferropicrites.

Reaction melting of pyroxenite and peridotite sources

The reaction between recycled oceanic crust (in the form of eclogite) and peridotite may produce silica-undersaturated garnet pyroxenite, which may ultimately represent the source of ferropicrites. The pyroxenite solidus is significantly lower than that of peridotite, and the mechanism of segregation of the first-formed melts and their subsequent interaction with the surrounding peridotite will greatly influence the final magma composition. Partial melts of basalt–peridotite sandwich experiments (Takahashi & Kushiro, 1983; Yaxley & Green, 1998; Takahashi & Nakajima, 2002) are silica-rich whereas

experiments on homogeneous mixtures of MORB and KLB-1 (Kogiso *et al.*, 1998) and GA1–MPY90 (Yaxley, 2000) have produced silica-undersaturated partial melts. This is because the bulk compositions of the basalt–peridotite mixtures are located on the silica-deficient side of the CaTs–En thermal divide (Fig. 15b). Yaxley (2000) suggested that if partial melts of eclogite were able to separate from their source region, they would be silica-rich and very reactive towards peridotite. The reactions would effectively redistribute the eclogite bodies and 'fertilize' the peridotite by enhancing the amount of garnet and pyroxene. Progressive mixing and reaction between the siliceous partial melts of eclogite and the surrounding peridotite would move the bulk composition of the re-fertilized peridotite towards that of a homogeneous eclogite–peridotite mixture. Olivine websterite (HK66) may have been formed by such a fertilization mechanism (see above). Subsequent melting may then produce silica-undersaturated partial melts. This mechanism might explain why ferropicrites have high bulk-Ni contents (e.g. 660 ppm in 97SB68), despite possibly being generated from an olivine-free garnet pyroxenite source. Reaction between siliceous partial melts of pyroxenite and Ni-rich peridotite may cause the elimination of olivine and subsequent incompatible behaviour of Ni, such that it would concentrate in the ferropicrite melt.

The reaction of eclogite partial melts with peridotite produces bands of orthopyroxene at the interface, which reduces reaction rates (Takahashi & Nakajima, 2002) and limits the amount of silica-undersaturated partial melts produced. Kogiso *et al.* (2004) have argued that infiltration of pyroxenite-derived partial melts into surrounding peridotite can occur only if the latter has finite permeability. They suggested that melts derived from silica-undersaturated garnet pyroxenite would dissolve orthopyroxene and permit reactive infiltration. They also proposed that melting of pyroxenite bodies several metres in thickness is required to retain the major and trace element, and isotope signature of the source in the primary melts. Only slow diffusing isotopic signatures would be preserved in melts derived from smaller pyroxenite bodies.

Generation of high-Fe melts in upwelling mantle plumes

Mantle plumes have been proposed to be associated with the genesis of ferropicrites worldwide (Gibson, 2002). These Fe-rich mantle melts have been observed only at the base of continental flood basalt (CFB) provinces and are apparently absent in ocean island basalt (OIB) successions. They are thought to represent high-pressure partial melts of upwelling mantle plumes that entrain recycled oceanic lithosphere, in the form of eclogite 'streaks'. The ferropicrites in the Paraná–Etendeka CFB province are found at the base of the succession and represent a relatively small volume of the erupted magma. They are believed to represent the earliest stages of mantle melting associated with the Early Cretaceous impact of the Tristan da Cunha mantle plume (Gibson *et al.*, 2000). There is no evidence for significant lithospheric thinning beneath the Etendeka region of NW Namibia at the time of genesis of the ferropicrites (Gibson *et al.*, 2000) and so in the following discussion we have assumed a mechanical boundary layer (MBL) thickness of ~125 km (McKenzie & Bickle, 1988).

As discussed above, the fractionated HREE (Fig. 18), low Al_2O_3 content (Table 1) and the phase relations of 97SB68 suggest that the primary ferropicrite melts separated from a garnet–pyroxene residue that may have formed through reaction of peridotite and eclogite at ≥5 GPa (i.e. 165 km; Fig. 4a). At these pressures, the ferropicrite liquidus is at ≥1650°C (Table 2) and this defines a minimum temperature for the solidus of the mantle source region. Figure 19 shows the solidus of fertile peridotite (KLB-1) and the solidus and liquidus of a silica-undersaturated garnet pyroxenite (MIX1G). Also shown is the 97SB68 ferropicrite liquidus from Fig. 4a. The dP/dT of the ferropicrite liquidus (3·75°C/kbar) is steeper than the adiabatic path of upwelling mantle (1°C/kbar) such that an adiabat with a potential temperature (T_p) of 1550°C, which is thought to be appropriate for impacting starting-mantle plume heads (McKenzie & O'Nions, 1991; White & McKenzie, 1995), intersects the liquidus at ~5 GPa (Fig. 19). An adiabat for a T_p of 1550°C intersects the mean estimate of the garnet pyroxenite solidus at ~5 GPa (~165 km), which is 50°C lower than the KLB-1 solidus. The relatively high bulk-K_2O content of 97SB68 (Table 1) and the inflection of the ferropicrite solidus in Fig. 4a suggest a source composition with a relatively high K_2O content. Such a source may experience a small degree of incipient melting at significantly greater depths than 165 km (see above). However, in an ascending plume with a T_p of ~1550°C, melting of pyroxenite would occur only at depths close to 165 km, where the adiabat intersects the garnet and pyroxene 'cotectic'; these phases would melt rapidly in approximately equal proportions over a small pressure–temperature interval (Figs 4b and 5). Increased upwelling of the plume would result in the intersection of the anhydrous peridotite solidus at ~150 km (Fig. 19) but a 125 km thick MBL would prevent significant subsequent melting. At this point (125 km), the pyroxenite would be almost completely molten or significant chemical reactions would have taken place with the surrounding peridotite.

After segregation from the mantle source region at ~165 km, the temperature of the ferropicrite melt would be ~1630°C, assuming a T_p of 1550°C (Fig. 19). During ascent through the lithosphere (Turcotte, 1987), the melt

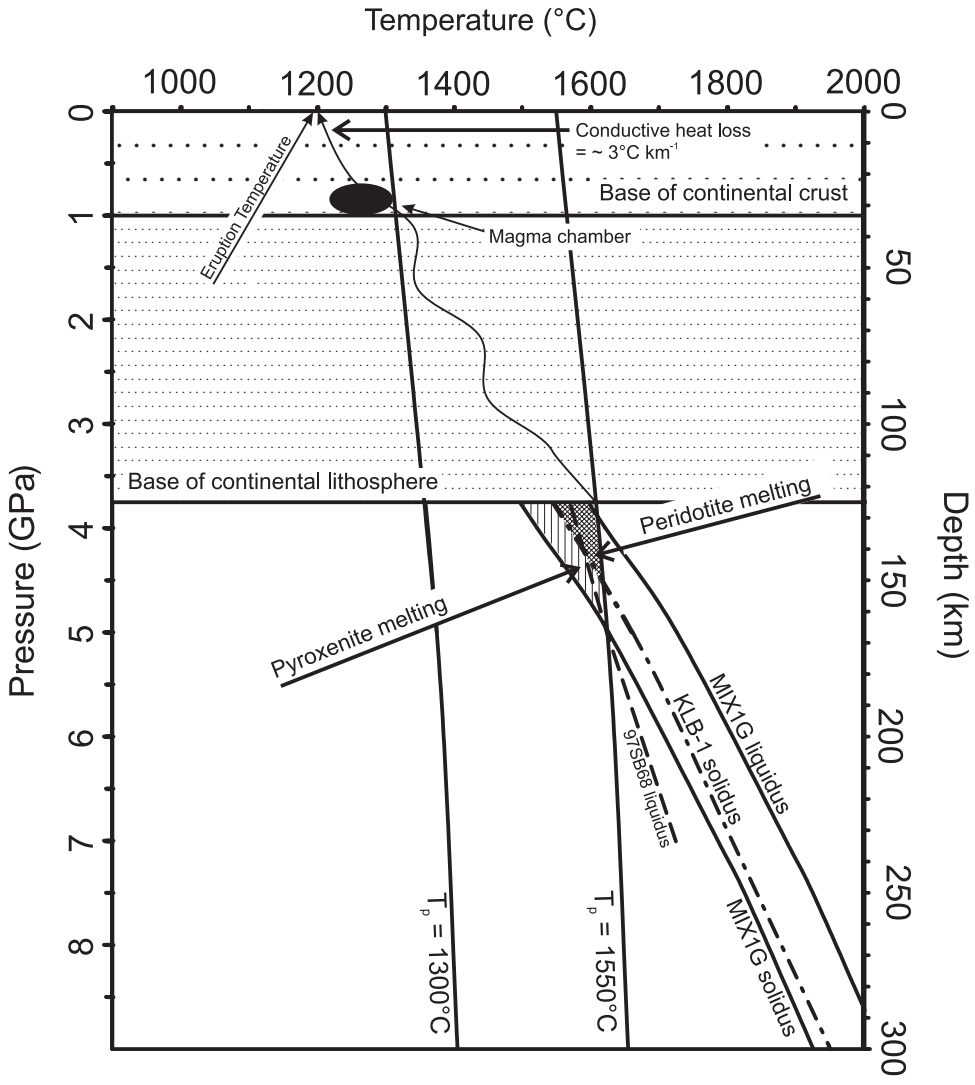

Fig. 19. *P–T* plot showing the solidi (±50°C) of peridotite KLB-1 (Takahashi *et al.*, 1993; Herzberg *et al.*, 2000; Hirschmann, 2000), MIX1G (Kogiso *et al.*, 2003) and the liquidus of 97SB68. Mantle potential temperature (T_p) adiabats of 1300°C, for ambient mantle and 1550°C, thought to be appropriate for impacting mantle plume starting heads (McKenzie & O'Nions, 1991; Watson & McKenzie, 1991; White & McKenzie, 1995) are also shown, along with the base of continental lithosphere at ~125 km (McKenzie & Bickle, 1988) and the base of continental crust at ~35 km.

would undergo conductive heat loss. As demonstrated in Fig. 4a, at ~1 GPa 97SB68 crystallizes olivine, then clinopyroxene and finally plagioclase, whereas plagioclase crystallizes before clinopyroxene in the same composition at 1 atm. A number of the more evolved Paraná–Etendeka ferropicrites were proposed by Gibson *et al.* (2000) to fractionate olivine and then clinopyroxene, prior to migration to the surface, at ~1 GPa in agreement with the sequence predicted by the ~1 GPa phase relations of 97SB68. The lack of feldspar phenocrysts indicates a surface eruption temperature of ~1200°C and this represents a conductive heat loss rate of ~3°C/km. This estimate is consistent with the value used by Scarrow & Cox (1995) for the high-Mg Skye lavas and is within the range for basic magmas ascending turbulently through the crust calculated by Huppert & Sparks (1985). A temperature of 1200°C represents a minimum eruption temperature for 97SB68 because it is among the most magnesian of the Paraná–Etendeka ferropicrites and does not display evidence of crystal fractionation (see Gibson *et al.*, 2000, fig. 7), i.e. we believe it erupted onto the surface soon after melt separation.

Evolution of the Tristan mantle plume and the development of thinner lithosphere (~70 km) may account for the huge volumes of flood basalts that were emplaced after the ferropicrites in the Paraná–Etendeka CFB province. The absence of a thick MBL would allow substantial upwelling of the mantle plume and greater amounts of peridotite partial melting. This may dilute the pyroxenite signature so that the lavas have the compositions of

'normal basalts'. This model is consistent with the proposal of Cordery *et al.* (1997) and Campbell (1998) that mantle plumes responsible for CFB volcanism require a significant eclogite component. Other workers (e.g. Yaxley, 2000) have proposed that peridotite melting alone cannot produce the large volumes of melt for even small CFBs, unless mantle potential temperatures are very high (T_p >1600°C).

During adiabatic decompression melting of a pyroxenite-bearing mantle plume beneath oceanic lithosphere, with a MBL of <100 km, a larger degree of peridotite partial melting would occur. This would cause greater dilution of the pyroxenite signature (Kogiso *et al.*, 2003) and may explain why Fe-rich melts have not been observed in OIB successions. Our model accounts for the limited occurrence of ferropicrite magmas at the base of CFB sequences and their absence in OIB successions. Formation of ferropicrite magmas in OIB successions may be impeded owing to the lack of thick lithosphere and/or may be rare because (1) OIBs do not represent the emplacement stage of the plume, and (2) the exposure is usually not deep enough in OIB sections to see the initial stage of magmatism.

CONCLUSIONS

The results of our 1 atm to 7 GPa experiments on a ferropicrite from the Paraná–Etendeka CFB have allowed us to make the following conclusions regarding the processes operating during the initial sub-lithospheric impact of the Tristan mantle plume.

(1) The results of our experiments suggest that the primary ferropicrite melts separated from either an olivine–clinopyroxene residue at ~2·2 GPa or a garnet–clinopyroxene residue at ≥5 GPa. Of these, high-pressure melting of a garnet–clinopyroxene-rich mantle is more plausible as the Paraná–Etendeka ferropicrites are characterized by low Al_2O_3 contents and fractionated HREE ratios. The ferropicrite phase relations contrast with those of Hawaiian picrites (Maaløe, 2004), which—at the time of melt separation—were in equilibrium with olivine and orthopyroxene.

(2) The ferropicrite composition is similar to 5 GPa melts of silica-undersaturated garnet pyroxenite. Experimental melts of the latter are, however, richer in CaO and lower in K_2O (Kogiso *et al.*, 2003). Melts of subducted MORB are silica-saturated and cannot account for the silica-undersaturated ferropicrites, unless they have reacted with the surrounding peridotite. This 'refertilization' process is thought to produce nepheline-normative partial melts (Yaxley, 2000). A source composition similar to a 75% basalt–25% peridotite mixture ($GA1_{75}MPY90_{25}$) appears to be the most appropriate but, unfortunately, no experimental data are available for pressures ≥5 GPa.

(3) At 5 GPa, the ferropicrite liquidus is at 1650°C, which is similar to the solidus of the silica-undersaturated garnet pyroxenite studied by Kogiso *et al.* (2003). At these pressures and temperatures, the garnet pyroxenite solidus would be intersected by an upwelling plume with a mantle potential temperature of 1550°C.

(4) The solidi of mafic rocks with sizeable amounts of K_2O drop significantly at 3–7 GPa but become identical to K-depleted rocks above ~8 GPa. K_2O is compatible in diopsidic clinopyroxene at >7 GPa (Tsurata & Takahashi, 1998). Small degrees of melting may have occurred in the ferropicrite source between 3 and 7 GPa, but formation of ferropicrite primary melts (such as 97SB68 with 0·68 wt % K_2O) would occur only at ~165 km depth in an upwelling plume with a T_p of 1550°C with the intersection of the garnet–clinopyroxene 'cotectic'.

(5) Subsequent upwelling and melting of the Tristan plume would be restricted by the thick overlying continental lithosphere. Intersection of the peridotite solidus would occur at ~4·5 GPa, for a T_p of 1550°C, and only limited melting would occur beneath a ~125 km thick lithosphere. More extensive peridotite melting, and hence dilution of garnet pyroxenite derived melts, would occur beneath thinner oceanic lithosphere and may explain the apparent absence of ferropicrites in intra-plate oceanic settings. Formation of ferropicrite magmas in OIB successions may be impeded owing to the lack of thick lithosphere and/or may be rare because (1) OIBs do not represent the emplacement stage of the plume, and (2) the exposure is usually not deep enough in OIB sections to see the initial stage of magmatism.

(6) The results of our study are in agreement with previous investigations, which have proposed that mantle plumes consist of both garnet pyroxenite and peridotite. The garnet pyroxenite may relate to the presence of subducted oceanic lithosphere that has been entrained within the upwelling plume and has reacted with the surrounding peridotite.

ACKNOWLEDGEMENTS

We are grateful to Professor M. J. Bickle and Dr Tetsu Kogiso for their perceptive comments on earlier versions of the manuscript. We are grateful to Professor R. N. Thompson for the samples used in this work. We are also grateful for the technical assistance and advice of Dr Toshihiro Suzuki and Dr Shingo Takeuchi. We thank Dr John Taylor, Corpus Christi College and the University of Cambridge for the support of J.T. during this research project. Laboratory work was supported by scientific grant in aid No. 12002006 from the Ministry of Education and Science, Japan to E.T. This is Department of Earth Sciences contribution ES 8113.

REFERENCES

Allègre, C. J. & Turcotte, D. L. (1986). Implications of a two-component marble-cake mantle. *Nature* **323**, 123–127.

Allègre, C. J., Brévart, O., Dupré, B. & Minster, J. F. (1980). Isotopic and chemical effects produced in a continuously differentiating convecting Earth mantle. *Philosophical Transactions of the Royal Society of London, Series A* **297**, 447–477.

Arndt, N. T. (1994). Archean komatiites. In: Condie, K. C. (ed.) *Archean Crustal Evolution*. New York: Elsevier, pp. 11–44.

Baker, M. B., Alves, S. & Stolper, E. M. (1996). Petrography and petrology of the Hawaii Scientific Drilling Project: inferences from olivine phenocryst abundances and compositions. *Journal of Geophysical Research* **101**, 11715–11728.

Bickle, M. J., Ford, C. E. & Nisbet, E. G. (1977). The petrogenesis of peridotitic komatiites: evidence from high-pressure melting experiments. *Earth and Planetary Science Letters* **37**, 97–106.

Bohlen, S. R. & Boettcher, A. L. (1982). The quartz–coesite transformation: a precise determination and the effects of other components. *Journal of Geophysical Research* **87**, 7073–7078.

Campbell, I. H. (1998). The mantle's chemical structure: insights from the melting products of mantle plumes. In: Jackson, I. (ed.) *The Earth's Mantle: Composition, Structure and Evolution*. Cambridge: Cambridge University Press, pp. 259–310.

Campbell, I. H. & Griffiths, R. W. (1990). Implications of mantle plume structure for the evolution of flood-basalts. *Earth and Planetary Science Letters* **99**, 79–93.

Campbell, I. H. & Griffiths, R. W. (1993). The evolution of the mantle's chemical structure. *Lithos* **30**, 389–399.

Cordery, M. J., Davies, G. F. & Campbell, I. H. (1997). Genesis of flood basalts from eclogite-bearing mantle plumes. *Journal of Geophysical Research* **102**, 20179–20197.

Cox, K. G. & Jamieson, B. G. (1974). The olivine-rich lavas of Nuanetsi: a study of polybaric magmatic evolution. *Journal of Petrology* **15**, 269–301.

Fram, M. S. & Lesher, C. E. (1997). Generation and polybaric differentiation of East Greenland Early Tertiary flood basalts. *Journal of Petrology* **38**, 231–275.

Garcia, M. O. (1996). Petrography and olivine glass chemistry of lavas from the Hawaii Scientific Drilling Project. *Journal of Geophysical Research* **101**, 11701–11715.

Gibson, S. A. (2002). Major element heterogeneity in Archean to Recent mantle plume starting-heads. *Earth and Planetary Science Letters* **195**, 59–74.

Gibson, S. A., Thompson, R. N., Leonardos, O. H., Dickin, A. P. & Mitchell, J. G. (1995). The Late Cretaceous impact of the Trinidade mantle plume: evidence from large-volume, mafic, potassic magmatism in SE Brazil. *Journal of Petrology* **36**, 189–229.

Gibson, S. A., Thompson, R. N., Dickin, A. P. & Leonardos, O. H. (1996). Erratum to 'High-Ti and low-Ti mafic potassic magmas: key to plume–lithosphere interactions and continental flood-basalt genesis'. *Earth and Planetary Science Letters* **141**, 325–341.

Gibson, S. A., Thompson, R. N. & Dickin, A. P. (2000). Ferropicrites: geochemical evidence for Fe-rich streaks in upwelling mantle plumes. *Earth and Planetary Science Letters* **174**, 355–374.

Green, D. H. & Ringwood, A. E. (1967). The genesis of basaltic magmas. *Contributions to Mineralogy and Petrology* **15**, 103–190.

Helffrich, G. R. & Wood, B. J. (2001). The Earth's mantle. *Nature* **412**, 501–507.

Herzberg, C. (1995). Generation of plume magmas through time—an experimental perspective. *Chemical Geology* **126**, 1–16.

Herzberg, C., Raterron, P. & Zhang, J. (2000). New experimental observations on the anhydrous solidus for peridotite KLB-1. *Geochemistry, Geophysics, Geosystems* **1**, 2000GC000089.

Hirose, K. & Kushiro, I. (1993). Partial melting of dry peridotites at high pressures—determination of compositions of melts segregated from peridotite using aggregates of diamond. *Earth and Planetary Science Letters* **114**, 477–489.

Hirschmann, M. M. (2000). Mantle solidus: experimental constraints and the effects of peridotite composition. *Geochemistry, Geophysics, Geosystems* **1**, 2000GC000070.

Hirschmann, M. M., Kogiso, T., Baker, M. B. & Stolper, E. M. (2003). Alkalic magmas generated by partial melting of garnet pyroxenite. *Geology* **31**, 481–484.

Holland, T. J. B. (1980). The reaction albite = jadeite + quartz determined experimentally in the range 600–1200°C. *American Mineralogist* **65**, 129–134.

Huppert, H. E. & Sparks, R. S. J. (1985). Cooling and contamination of mafic and ultramafic magmas during ascent through continental crust. *Earth and Planetary Science Letters* **74**, 371–386.

Ito, E. & Takahashi, E. (1987). Melting of peridotite at uppermost lower-mantle conditions. *Nature* **328**, 514–517.

Jaques, A. L. & Green, D. H. (1980). Anhydrous partial melting of peridotite at 0–15 kb pressure and the genesis of tholeiitic basalts. *Contributions to Mineralogy and Petrology* **73**, 287–310.

Kamanetsky, V. S., Sobolev, A. V., Joron, J.-L. & Semet, M. P. (1995). Petrology and geochemistry of Cretaceous ultramafic volcanics from eastern Kamchatka. *Journal of Petrology* **36**, 637–662.

Kaneshima, S. & Helffrich, G. (1998). Detection of lower mantle scatterers northeast of the Mariana subduction zone using short-period array data. *Journal of Geophysical Research* **103**, 4825–4838.

Kaneshima, S. & Helffrich, G. (1999). Dipping low-velocity layer in the mid–lower mantle: evidence for geochemical heterogeneity. *Science* **283**, 1888–1891.

Kellogg, L. H., Hager, B. H. & van der Hilst, R. D. (1999). Compositional stratification in the deep mantle. *Science* **283**, 1881–1884.

Kogiso, T. & Hirschmann, M. M. (2001). Experimental study of clinopyroxenite partial melting and the origin of ultra-calcic melt inclusions. *Contributions to Mineralogy and Petrology* **142**, 347–360.

Kogiso, T., Hirose, K. & Takahashi, E. (1998). Melting experiments on homogeneous mixtures of peridotite and basalt: application to the genesis of ocean island basalts. *Earth and Planetary Science Letters* **162**, 45–61.

Kogiso, T., Hirschmann, M. M. & Frost, D. J. (2003). High-pressure partial melting of garnet pyroxenite: possible mafic lithologies in the source of ocean island basalts. *Earth and Planetary Science Letters* **216**, 603–617.

Kogiso, T., Hirschmann, M. M. & Reiners, P. W. (2004). Length scales of mantle heterogeneities constrained by basalt geochemistry. *Geochimica et Cosmochimica Acta* **68**, 345–360.

Kornprobst, J. (1977). A subsolidus high-pressure/high-temperature experimental study on a garnet-websterite assemblage exsolved from a single clinopyroxene accumulate at Freychinede (an alpine-type peridotite body, northern French Pyrénées). *Colloques Internationaux du CNRS* **272**.

Kuno, H. & Aoki, K. (1970). Chemistry of ultramafic nodules and their bearing on the origin of basaltic magmas. *Physics of the Earth and Planetary Interiors* **3**, 427–436.

Kushiro, I. (1969). Discussion of the paper 'The origin of basaltic and nephelinitic magmas in the Earth's mantle' by D. H. Green. *Tectonophysics* **7**, 427–436.

Kushiro, I. (1996). Partial melting of a fertile mantle peridotite at high pressures: an experimental study using aggregates of diamond.

In: Basu, A. & Hart, S. (eds) *Earth Processes: Reading the Isotopic Code. Geophysical Monograph, American Geophysical Union* **95**, 109–122.

Leitch, A. M. & Davies, G. F. (2001). Mantle plumes and flood basalts: enhanced melting from plume ascent and an eclogite component. *Journal of Geophysical Research* **106**, 2047–2059.

Lightfoot, P. C., Hawkesworth, C. J., Olshefsky, K., Green, T., Doherty, W. & Keays, R. R. (1997). Geochemistry of Tertiary tholeiites and picrites from Qeqertarssuaq (Disko Island) and Nuussuaq, West Greenland with implications for the mineral potential of comagmatic intrusions. *Contributions to Mineralogy and Petrology* **128**, 139–163.

Maaløe, S. (2004). The *PT*-phase relations of an MgO-rich Hawaiian tholeiite: the compositions of primary Hawaiian tholeiites. *Contributions to Mineralogy and Petrology* **148**, 236–246.

Matsukage, K. N. & Kubo, K. (2003). Chromian spinel during melting experiments of dry peridotite (KLB-1) at 1·0–2·5 GPa. *American Mineralogist* **88**, 1271–1278.

McKenzie, D. & Bickle, M. J. (1988). The volume and composition of melt generated by extension of the lithosphere. *Journal of Petrology* **29**, 625–679.

McKenzie, D. & O'Nions, R. K. (1991). Partial melt distributions from inversion of rare earth element concentrations. *Journal of Petrology* **32**, 1021–1091.

Norman, M. D. & Garcia, M. O. (1999). Primitive magmas and source characteristics of the Hawaiian plume: petrology and geochemistry of shield picrites. *Earth and Planetary Science Letters* **168**, 27–44.

O'Hara, M. J. (1968). The bearing of phase equilibria studies in synthetic and natural systems on the origin and evolution of basic and ultrabasic rocks. *Earth-Science Reviews* **4**, 69–133.

Parman, S. W., Dann, J. C., Grove, T. L. & de Wit, M. J. (1997). Emplacement conditions of komatiite magmas from the 3·49 Ga Komati Formation, Barberton Greenstone Belt, South Africa. *Earth and Planetary Science Letters* **150**, 303–323.

Peate, D. W. (1990). Stratigraphy and petrogenesis of the Paraná continental flood-basalts, southern Brazil. Ph.D. thesis, Open University, Milton Keynes, UK.

Pertermann, M. & Hirschmann, M. M. (2003*a*). Partial melting experiments on a MORB-like pyroxenite between 2 and 3 GPa: constraints on the presence of pyroxenite in basalt source regions from solidus location and melting rate. *Journal of Geophysical Research* **108**, 2125–2142.

Pertermann, M. & Hirschmann, M. M. (2003*b*). Anhydrous partial melting experiments on MORB-like eclogite: phase relations, phase compositions and mineral–melt partitioning of major elements at 2–3 GPa. *Journal of Petrology* **44**, 2173–2201.

Renne, P. R., Glen, J. M., Milner, S. C. & Duncan, A. R. (1997). Geochronology of the Paraná–Etendeka magmatic province. *EOS Transactions, American Geophysical Union* **78**, F472.

Renner, R. (1989). Cooling and crystallisation of komatiite flows from Zimbabwe. Ph.D. thesis, University of Cambridge, Cambridge, 162 pp.

Scarfe, C. M. & Takahashi, E. (1986). Melting of garnet peridotite to 13 GPa and the early history of the upper mantle. *Nature* **322**, 354–356.

Scarrow, J. H. & Cox, K. G. (1995). Basalts generated by decompressive adiabatic melting of a mantle plume: a case study from the Isle of Skye, NW Scotland. *Journal of Petrology* **36**, 3–22.

Shervais, J. W. & Mukasa, S. B. (1991). The Balmuccia orogenic lherzolites massif, Italy. *Journal of Petrology*, Special Lherzolites Issue, 155–176.

Silver, P. G., Carlson, R. W. & Olson, P. (1988). Deep slabs, geochemical heterogeneity, and the large-scale structure of mantle convection: investigation of an enduring paradox. *Annual Review of Earth and Planetary Sciences* **16**, 477–541.

Takahashi, E. (1986). Melting of a dry peridotite KLB-1 up to 14 GPa: implications on the origin of peridotitic upper mantle. *Journal of Geophysical Research* **91**, 9367–9382.

Takahashi, E. & Kushiro, I. (1983). Melting of a dry peridotite at high pressures and basalt magma genesis. *American Mineralogist* **68**, 859–879.

Takahashi, E. & Nakajima, K. (2002). Melting process in the Hawaiian plume: an experimental study. In: Takahashi, E., Lipman, P. W., Garcia, M. O., Naka, J. & Aramaki, S. (eds) *Hawaiian Volcanoes: Deep Underwater Perspectives. Geophysical Monograph, American Geophysical Union* **128**, 403–418.

Takahashi, E. & Scarfe, C. M. (1985). Melting of peridotite to 14 GPa and the genesis of komatiite. *Nature* **315**, 566–568.

Takahashi, E., Yamada, H. & Ito, E. (1982). An ultrahigh-pressure furnace assembly to 100 kbar and 1500°C with minimum temperature uncertainty. *Geophysical Research Letters* **9**, 805–807.

Takahashi, E., Shimazaki, T., Tsuzaki, Y. & Yoshida, H. (1993). Melting study of a peridotite KLB-1 to 6·5 GPa, and the origin of basaltic magmas. *Philosophical Transactions of the Royal Society of London, Series A* **342**, 105–120.

Takahashi, E., Nakajima, K. & Wright, T. L. (1998). Origin of the Columbia River basalts: melting model of a heterogeneous plume head. *Earth and Planetary Science Letters* **162**, 63–80.

Thompson, R. N. (1975). Primary basalts and magma genesis II. Snake River Plain, Idaho, U.S.A. *Contributions to Mineralogy and Petrology* **52**, 213–232.

Thompson, R. N. & Gibson, S. A. (2000). Transient high temperatures in mantle plume heads inferred from magnesian olivines in Phanerozoic picrites. *Nature* **407**, 502–505.

Thompson, R. N., Gibson, S. A., Dickin, A. P. & Smith, P. M. (2001). Early Cretaceous basalt and picrite dykes of the southern Etendeka region, NW Namibia: windows into the role of the Tristan mantle plume in Paraná–Etendeka magmatism. *Journal of Petrology* **42**, 2049–2081.

Tsuruta, K. & Takahashi, E. (1998). Melting study of an alkali basalt JB-1 up to 12·5 GPa: behaviour of potassium in the deep mantle. *Physics of the Earth and Planetary Interiors* **107**, 119–130.

Turcotte, D. L. (1987). Physics of magma segregation processes. In: Mysen, O. B. (ed.) *Magmatic Processes: Physiochemical Principles. Geochemical Society, Special Publication* **1**, 69–74.

Ulmer, P. (1989). The dependence of the Fe^{2+}–Mg cation-partitioning between olivine and basaltic liquid on pressure, temperature and composition—an experimental study to 30 kbars. *Contributions to Mineralogy and Petrology* **101**, 261–273.

Van Heerden, L. A. & Le Roex, A. P. (1988). Petrogenesis of picrite and associated basalts from the southern mid-Atlantic ridge. *Contributions to Mineralogy and Petrology* **100**, 47–60.

Walter, M. J. (1998). Melting of garnet peridotite and the origin of komatiite and depleted lithosphere. *Journal of Petrology* **39**, 29–60.

Wang, W. & Takahashi, E. (1999). Subsolidus and melting experiments of a K-rich basaltic composition to 27 GPa: implication for the behaviour of potassium in the mantle. *American Mineralogist* **84**, 357–361.

Wang, W. & Takahashi, E. (2000). Subsolidus and melting experiments of K-doped peridotite KLB-1 to 27 GPa: its geophysical and geochemical implications. *Journal of Geophysical Research* **105**, 2855–2868.

Watson, S. & McKenzie, D. (1991). Melt generation by plumes—a study of Hawaiian volcanism. *Journal of Petrology* **32**, 501–537.

Wei, K., Tronnes, R. G. & Scarfe, C. M. (1990). Phase relations of aluminum-undepleted and aluminum-depleted komatiites at pressures of 4–12 GPa. *Journal of Geophysical Research* **95**, 15817–15827.

White, R. S. & McKenzie, D. (1995). Mantle plumes and flood basalts. *Journal of Geophysical Research* **100**, 17543–17585.

Wooden, J. L., Czamanske, G. K., Fedorenko, V. A., Arndt, N. T., Chauvel, C., Bouse, R. M., King, W. B. S., Knight, R. J. & Siems, D. F. (1993). Isotopic and trace-element constraints on mantle and crustal contributions to Siberian continental flood basalts, Noril'sk area, Siberia. *Geochimica et Cosmochimica Act* **57**, 3677–3704.

Yasuda, A., Fujii, T. & Kurita, K. (1994). Melting phase relations of an anhydrous mid-ocean ridge basalt from 3 to 20 GPa: implications for the behaviour of subducted oceanic crust in the mantle. *Journal of Geophysical Research* **99**, 9401–9414.

Yaxley, G. M. (2000). Experimental study of the phase and melting relations of homogeneous basalt + peridotite mixtures and implications for the petrogenesis of flood basalts. *Contributions to Mineralogy and Petrology* **139**, 326–338.

Yaxley, G. M. & Green, D. H. (1998). Reactions between eclogite and peridotite: mantle refertilisation by subduction of oceanic crust. *Schweizerische Mineralogische und Petrographische Mitteilungen* **78**, 243–255.

Zhang, J. & Herzberg, C. (1994). Melting experiments on anhydrous peridotite KLB-1 from 5·0 to 22·5 GPa. *Journal of Geophysical Research* **99**(B9), 17729–17742.

Zhao, D. (2001). Seismic structure and origin of hotspots and mantle plumes. *Earth and Planetary Science Letters* **192**, 251–265.